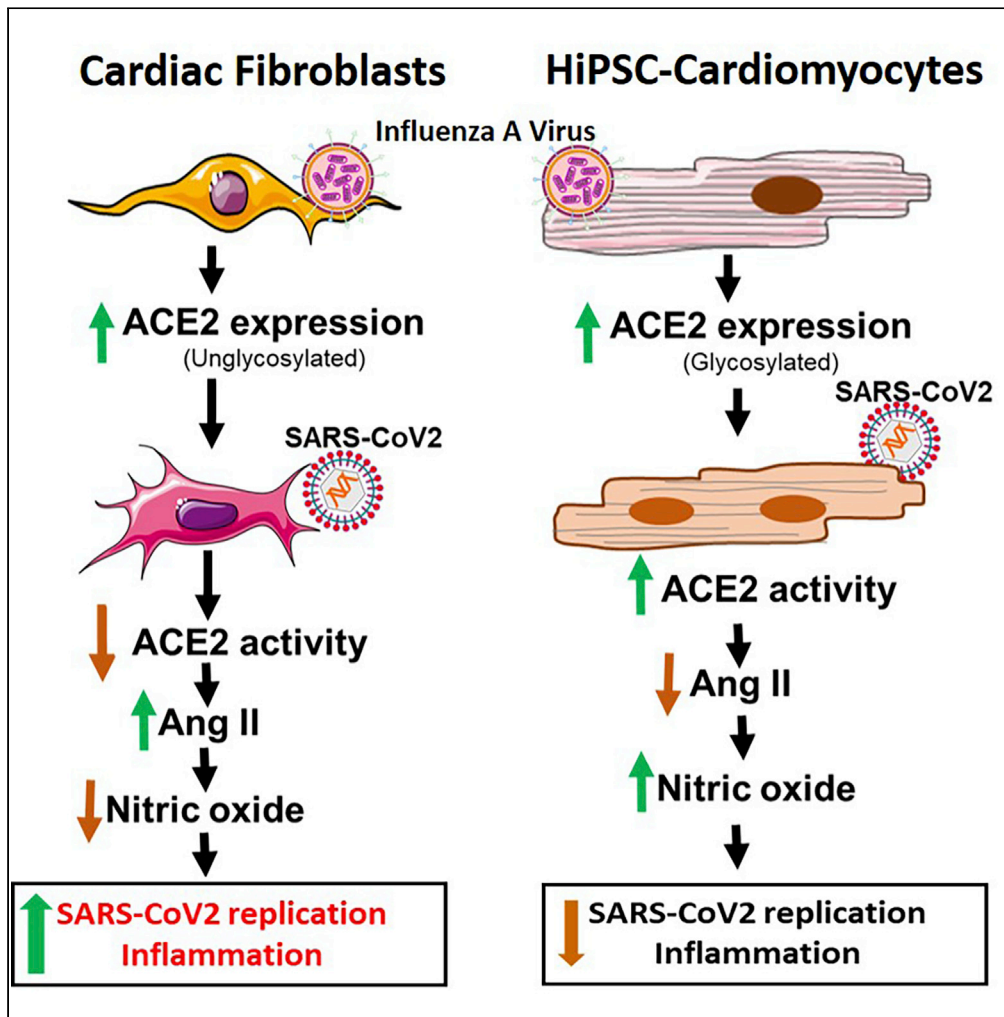## Article

# Influenza A virus modulates ACE2 expression and SARS-CoV-2 infectivity in human cardiomyocytes



Qian Wu, Naresh Kumar, William P. Lafuse, ..., Latha P. Ganesan, Jacob S. Yount, Murugesan V.S. Rajaram

murugesan.rajaram@osumc. edu

### Highlights

IAV infection enhances the expression of ACE2, a receptor for SARS-CoV2

Both IAV and IBV infection enhances the expression of ACE2 in human and mouse lungs

IAV induced glycosylated ACE2 in hiPSC-CMs restrict SARS-CoV2 replication

IAV and SARS-CoV2 co-infection increases mortality in a mouse model of infection

# iScience

## Article

# Influenza A virus modulates ACE2 expression and SARS-CoV-2 infectivity in human cardiomyocytes

Qian Wu,[1,8] Naresh Kumar,[1,8] William P. Lafuse,[1,8] Omar Santiagonunez Ahumada,[1] Noushin Saljoughian,[1] Elizabeth Whetstone,[1] Ashley Zani,[1] Ashley K. Patton,[2] Mona El Refaey,[3] Amy Webb,[4] Maciej Pietrzak,[4] Lianbo Yu,[4] Mahesh KC,[5,6] Mark E. Peeples,[5,6] Latha P. Ganesan,[7] Jacob S. Yount,[1] and Murugesan V.S. Rajaram[1,9,*]

## SUMMARY

**Influenza A virus (IAV) and SARS-CoV-2 virus are both acute respiratory viruses currently circulating in the human population. This study aims to determine the impact of IAV infection on SARS-CoV-2 pathogenesis and cardiomyocyte function. Infection of human bronchial epithelial cells (HBEC), A549 cells, lung fibroblasts (HLF), monocyte derived macrophages (MDMs), cardiac fibroblasts (HCF) and hiPSC-derived cardiomyocytes with IAV enhanced the expression of ACE2, the SARS-CoV-2 receptor. Similarly, IAV infection increased levels of ACE2 in the lungs of mice and humans. Of interest, we detected heavily glycosylated form of ACE2 in hiPSC-CMs and poorly glycosylated ACE2 in other cell types. Also, prior IAV infection enhances SARS-CoV-2 spike protein binding and viral entry in all cell types. However, efficient SARS-CoV-2 replication was uniquely inhibited in cardiomyocytes. Glycosylation of ACE2 correlated with enzymatic conversion of its substrate Ang II, induction of eNOS and nitric oxide production, may provide a potential mechanism for the restricted SARS-CoV-2 replication in cardiomyocytes.**

## INTRODUCTION

Severe acute respiratory syndrome coronavirus 2 (SARS-CoV-2) infections, and the resulting disease known as COVID-19, have led to millions of deaths worldwide. Although COVID-19 is primarily a respiratory infection, extra pulmonary complications have become well characterized in severe cases. Indeed, cardio-vascular damage caused by infection plays a critical role in morbidity and mortality. Numerous studies have reported an elevated level of cardiac troponin, an indicator of cardiac damage, and abnormalities in heart function in COVID-19 patients.[1–3] Other cardiovascular complications associated with COVID-19 include myocarditis, acute myocardial infarction, heart failure, and arrhythmias.[4,5] The mechanisms underlying such pulmonary and cardiac tissue injury are poorly understood.

In this regard, the extent to which other circulating infectious agents can influence the disease features of COVID-19 is also largely unknown. To date, there is limited evidence for co-infections with respiratory bacteria in severe COVID-19 patients.[6] By contrast, viral coinfections have been more commonly detected, including infections with rhinovirus, respiratory syncytial virus, and common cold coronaviruses.[7] Coinfection of influenza A virus (IAV) has also reported in several COVID-19 cases with poor outcome.[8,9] In a mouse model, IAV significantly elevated expression of the SARS-CoV-2 receptor, angiotensin-converting enzyme 2 (ACE2), in the lungs, thereby promoting infection.[10,11] ACE2 is expressed in many tissues throughout the body, potentially allowing SARS-CoV-2 to infect a wide range of cell types, including type 2 pneumocytes in the lung as well as cardiac fibroblasts and cardiomyocytes in the heart.[12–14] Also, we have demonstrated that IAV disseminates to the heart tissue and causes cardiac fibrosis and electrical dysfunction.[15] Thus, we wanted to determine whether IAV infection regulates ACE2 and consequent SARS-CoV-2 infectivity in human cardiac cells. Understanding the mechanism of IAV coinfection and SARS-CoV-2 pathogenesis in cardiac cells might help explain some cases of COVID-19 that involve cardiac problems and might provide the opportunity to protect the heart from SARS-CoV-2 infection.

ACE2 plays a major role in the renin-angiotensin system (RAS), in which it regulates levels of angiotensin II (Ang II) through proteolytic processing of Ang II to angiotensin (1–7), which serves as an Ang II antagonist.[16]

[1]Department of Microbial Infection and Immunity, Abigail Wexner Research Institute, Nationwide Children's Hospital, Columbus, OH 43209, USA

[2]Department of Pathology, Abigail Wexner Research Institute, Nationwide Children's Hospital, Columbus, OH 43209, USA

[3]Department of Surgery, Abigail Wexner Research Institute, Nationwide Children's Hospital, Columbus, OH 43209, USA

[4]Department of Biomedical Informatics, Abigail Wexner Research Institute, Nationwide Children's Hospital, Columbus, OH 43209, USA

[5]Department of Pediatrics, Abigail Wexner Research Institute, Nationwide Children's Hospital, Columbus, OH 43209, USA

[6]Center for Vaccines and Immunity, Abigail Wexner Research Institute, Nationwide Children's Hospital, Columbus, OH 43209, USA

[7]Department of Internal Medicine College of Medicine, The Ohio State University, Wexner Medical Center, Columbus, OH 43210, USA

[8]These authors contributed equally

[9]Lead contact

*Correspondence: murugesan.rajaram@osumc.edu

https://doi.org/10.1016/j.isci.2022.105701

Ang II binds primarily to receptors, affecting signaling cascades that regulate tissue remodeling, acute vasoconstriction, fibrosis, apoptosis, inflammation and hypertrophy.[17,18] ACE2 glycosylation is essential for the enzymatic conversion of Ang II into Ang (1–7). ACE2 can be heavily glycosylated in cells, with seven potential N-linked glycosylation sites and one O-linked glycosylation site[19] and molecular dynamic simulation studies indicate that two of the glycosylation sites, N90 and N332, have opposite effects on binding of the spike receptor domain (RBD).[20] Glycosylation of N90 partially covers and interferes with binding at the spike-ACE2 interface. Although studies of ACE2 in transfected human embryonic kidney (HEK293) cells have outlined the role of its N-glycans in SARS-CoV-2 interactions, glycosylation and effects of this modification has not been well characterized in pulmonary and cardiac cell types.

In this study we identify the mechanism by which IAV pre-infection modulates ACE2 expression and its glycosylation state, thereby dictating susceptibility to SARS-CoV-2 in various cell types. We show that as a result of ACE2 glycosylation, downstream events including peptidase activity, eNOS expression and nitric oxide production lead to the inhibition of SARS-CoV-2 replication in cardiomyocytes, but not in the lungs. This data strongly suggests that IAV infection may enhance the severity of SARS-CoV-2 infection in the lungs, posing a severe risk to public health.

## RESULTS

### Influenza A virus infection enhances expression of ACE2

We first determined whether IAV enhances ACE2 or TMPRSS2 expression, host proteins that are required for SARS-CoV-2 entry into lung and cardiac cells. These cells included a human pneumocyte-like epithelial cell line (A549), human lung fibroblast cells (HLF), human primary cardiac fibroblasts (HCF), and human induced pluripotent stem cell derived cardiomyocytes (hiPSC-CMs). Western blotting for ACE2 showed that ACE2 is poorly expressed in uninfected A549, HCF and HLF cells, but highly up-regulated by IAV in A549 (Figure 1A), HCF (Figure 1B) and HLF (Figure S1A). Furthermore, we found that hiPSC-CMs have a basal level of ACE2 that is further increased following IAV infection (Figure 1C). ACE2 levels quantified by Image J software are presented in the bottom panel.

Because lung tissue, the primary site of SARS-CoV-2 infection, is comprised principally of epithelial cells but also houses a large number of fibroblasts and macrophages, we separately assessed primary human bron-chial epithelial cultures (HBEC), human fibroblasts (HLF) and human monocyte derived macrophages (hMDMs) to determine whether IAV infection enhances ACE2 expression in these cell types. Similar to hiPSC-CMs, both HBEC and hMDMs had low levels of ACE2 expression, which were increased by IAV infection (Figure S1). IAV-induced cytotoxicity was quantified with the lactose dehydrogenase assay of the cell culture supernatants from IAV-infected HCF and hiPSC-CM cells. We found that IAV infection induced the death of HCF cells (28% at 48h and 42% at 72h). In contrast, IAV did not cause cytotoxicity in hiPSC-CMs until 72h post infection (Figure S2), suggesting that hiPSC-CMs are more resistant to IAV infection or IAV-induced cytotoxicity.

We next examined whether IAV infection alters the expression of TMPRSS2 in A549, HCF, and hiPSC-CMs. We found that IAV infection did not change the level of TMPRSS2 expression in any of these three cell types (Figure S3). To test whether the ACE2 induction is specific to influenza viruses, we exposed A549 cells to human metapneumovirus (MPV), or Sendai virus (SeV), or IAV and quantified ACE2 protein levels. IAV and MPV induced ACE2 expression, however, SeV did not (Figure S4).

We inoculated A549 cells with a variety of influenza strains (PR8, PR8-ΔNS1, H1N1, H3N2 and IBV) and examined ACE2 expression. We found that the highly pathogenic influenza strains (H1N1 and H3N2) are capable of inducing the ACE2 protein (Figue S4). Although, ACE2 is primarily localized in the plasma membrane, cleaved ACE2 can be internalized and localized in the cytoplasm, and viral infection can enhance the endocytosis of cleaved ACE2.[21] Thus, we determined the cellular localization of IAV-induced ACE2. We performed immunofluorescence microscopy using ACE2 specific antibody. Confocal micro-scopy of A549 (Figure 1D) and HCF cells (Figure 1E) confirmed that most of the ACE2 immunostaining was restricted to the cell surface. However, in hiPSC-CM cells (Figure 1F), ACE2 resides both in the outer membrane and intracellularly. Furthermore, we found that an increased expression of ACE2 in both IAV infected (high magnitude) and bystander cells (less magnitude). To confirm IAV infections in these experiments, we stained the cells with anti-Flu nucleoprotein antibody (green). The graphs shown in Figures 1G–1I are the quantification of ACE2 staining in IAV-infected cells. Together this data strongly
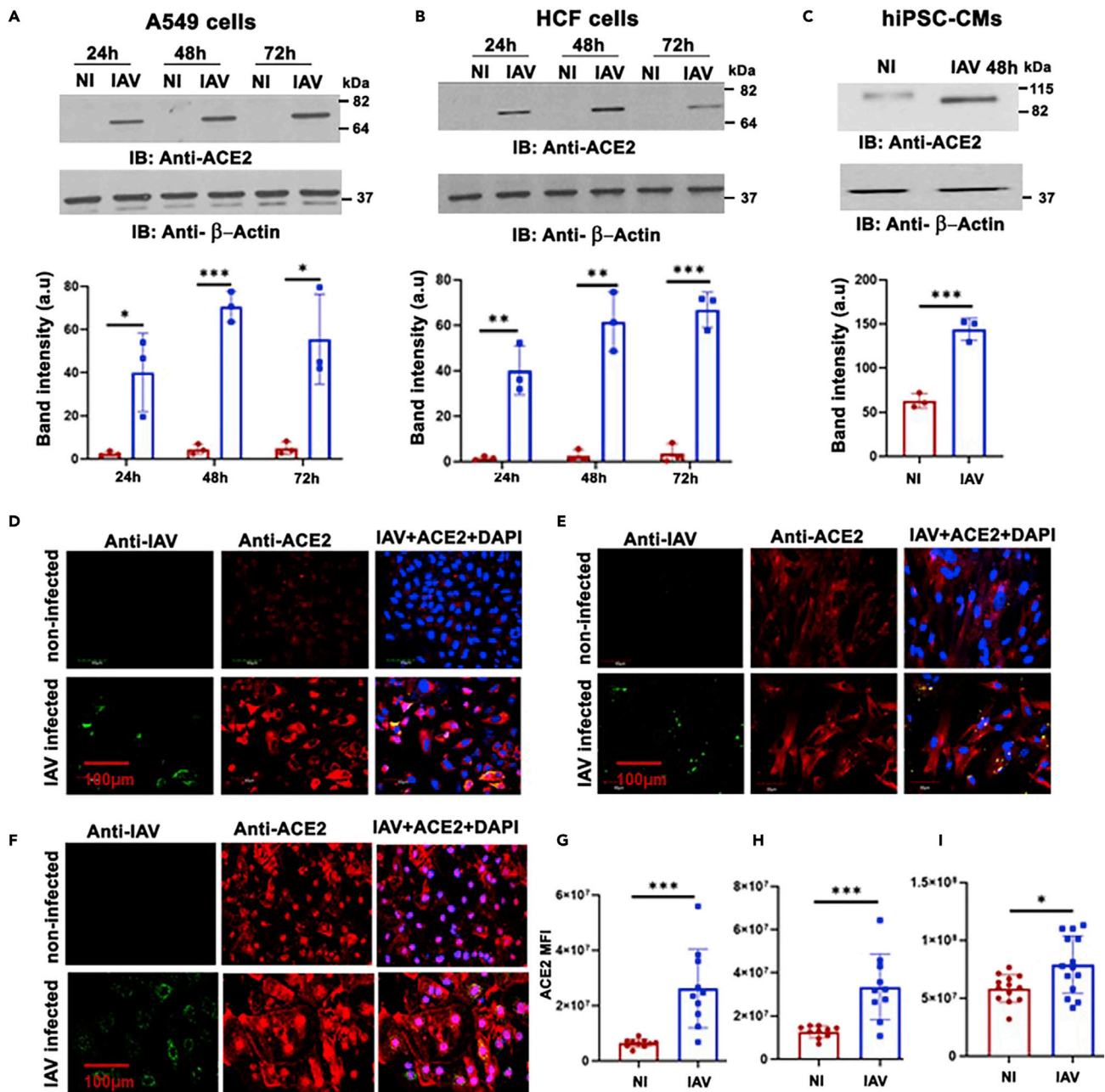
**Figure 1. Influenza A virus infection enhances the ACE2 expression in cardiac cells**

(A) Human lung epithelial A549 cells, (B) human cardiac fibroblast cells (HCF) and (C) hiPSC-CMs were exposed to IAV infection (1 MOI). After the indicated time points (24, 48 and 72h) cells were lysed and lysates containing equal amounts of protein were subjected to IB analysis with anti-ACE2 and anti β-actin antibodies. (D–F) A549, HCF and hiPSC-CMs were infected with IAV (1 MOI) or left uninfected. After 48h, the cells were fixed and stained with anti-IAV and anti ACE2 antibodies followed by AF488 and AF594 conjugated secondary antibodies respectively. The nuclei were stained with DAPI. Confocal images (scale bar = 100μm) shown in top panel are representative images of uninfected cells and images in the bottom panel are IAV infected cells (n = 3). The ACE2 staining (red) was quantified using Photoshop CC color range selection mode. The total intensity of the stained area was further evaluated via ImageJ using color intensity. (G–I) Graphs shown in G (A549), H (HCF) and I (hiPSC-CMs) are cumulative from 10 different images from 3 independent experiments. A two-tailed Student's t-test was used to analyze the data (mean ± *SEM*; **p< 0.005).

indicate that IAV infection enhances the expression of ACE2 in A549, HCF, hiPSC-CMs, HLF, hMDMs and HBECs and that in those cells tested (A549, HCF, and to a lesser extent hiPSC-CM) the expression is mainly on the cell surface.

To further examine whether IAV infection induces the expression of ACE2 and dACE2 mRNA, we measured the mRNA levels of ACE2 and dACE2 using previously described specific primers for the two isoforms.[22] Our results indicate that IAV infection induces the expression of both ACE2 and dACE2 mRNA in A549 (Figures S5A and S5B), HCF cells (Figures 5C and 5D) and in hiPSC-CMs (Figures 5E and 5F). Although IAV induced both forms of ACE2 in these cells, expression of dACE2 mRNA was 5–8 fold higher than ACE2 mRNA (Figure 5). However, dACE2 mRNA is reportedly not translated into a stable protein.[23] Nonetheless, we observed that dACE2 and ACE2 are both transcriptionally upregulated on IAV infection.

### Full length, fully glycosylated ACE2 is constitutively expressed in hiPSC-CM and vero cells

Recently, a novel isoform of ACE2, designated delta-ACE2 (dACE2) was described that lacks the 356 N-terminal amino acids of ACE2 and is, for that reason, defective in its carboxypeptidase activity and unable to bind SARS-CoV-2.[22–24] To avoid detection of the non-functional form in our immunoblot analyses, we used an antibody against the N-terminal region of ACE2, which does not detect the N-terminally deleted ACE2 species. Using this antibody, we detected the 110 kDa ACE2 protein in hiPSC-CM and Vero cells, both before and after IAV infection (Figure 1).

Non-glycosylated ACE2 is predicted to have a molecular mass of 78 kDa. The ACE2 sequence has seven N-linked glycosylation sites and one O-linked glycosylation site.[19] To confirm that the higher molecular mass of ACE2 in Vero and hiPSC-CMs is because of glycosylation, we incubated cell lysates with PNGase F before immunoblotting. The enzymatic deglycosylation decreased the molecular mass of ACE2 in Vero and hiPSC-CM cells (Figures 2B and 2C) to a size similar to that observed in IAV-infected A549 and HCF cells. Together this data strongly indicates that the larger molecular weight of ACE2 in Vero and hiPSC-CM cells is because of glycosylation and that most, if not all, of the predicted glycosylation sites are used. Of interest, neither A549 cells nor HCF cells expressed detectable ACE2 protein until they were infected by IAV. Furthermore, the ACE2 protein they expressed was 78 kDa, not 110 kDa, suggesting either that it was truncated, not glycosylated, or both. We also found ACE2 migrated as a slightly smaller species in IAV-infected hiPSC-CM compared to uninfected cells (Figure 2A). This reduction in size is likely because of the IAV neuraminidase glycoprotein which enzymatically removes the terminal sialic acid residues from the glycan's on glycoproteins.

Next, we examined whether glycosylation of ACE2 is critical for its peptidase activity. The cell lysates from uninfected and IAV-infected A549, HCF, Vero (susceptible to SARS-CoV-2) and hiPSC-CMs were subjected to an enzymatic peptidase assay using synthetic MCA based substrate. We found that cell lysates from Vero and hiPSC-CMs showed peptidase activity, correlating with the expression level of the highly glycosylated form of ACE2 (Figure 2D). Furthermore, hiPSC-CMs displayed higher ACE2 enzymatic activity after IAV infection suggesting that IAV upregulated the glycosylated ACE2. In contrast, we did not detect ACE2 enzymatic activity in A549 or HCF lysates even when derived from IAV-infected cells (Figure 2D), consistent with the idea that glycosylation is required for efficient peptidase activity.[25]

Because ACE2 in IAV-infected A549 and HCF cells is poorly glycosylated and lacks peptidase activity, we next determined whether ACE2 in IAV-infected A549 and HCF cells are capable of binding to the receptor binding domain (RBD) of the SARS-CoV-2 spike protein. A549 and HCF cells were infected with IAV or left uninfected for 48 h and then incubated with biotinylated-RBD, followed by AF488 conjugated streptavidin and examined by confocal microscopy. IAV infection increased the expression of ACE2 (Figures 2E and 2F), and increased binding of RBD. Both appeared to bind to the cell surface. These findings suggest that ACE2 glycosylation is not required for the RBD of the spike protein to bind to ACE2.

### IAV infection enhances the expression of ACE2 in the lungs and hearts of mice

To determine if IAV induces ACE2 expression *in vivo*, we examined the expression of ACE2 in lungs and heart tissue from mice infected with IAV. Confocal microscopy imaging showed that the expression of ACE2 was enhanced in lung sections from IAV-infected mice (Figure 3A). Furthermore, to identify the cell types, we co-stained the lung sections with SP-C antibody (marker for type II alveolar epithelial cells) and F4/80 (macrophages). Our results indicate that IAV infection in mice enhanced the expression of ACE2 primarily in type II epithelial cells (Figure 3A) but also in macrophages to some extent (Figure S6). Because we have previously shown that intranasal delivery of IAV disseminated into the heart tissue and caused cardiac fibrosis and electrical dysfunction.[15] Next, we examined the expression of ACE2 mRNA in heart tissue. Total RNA was extracted from IAV-infected and uninfected mice and ACE2 was quantified
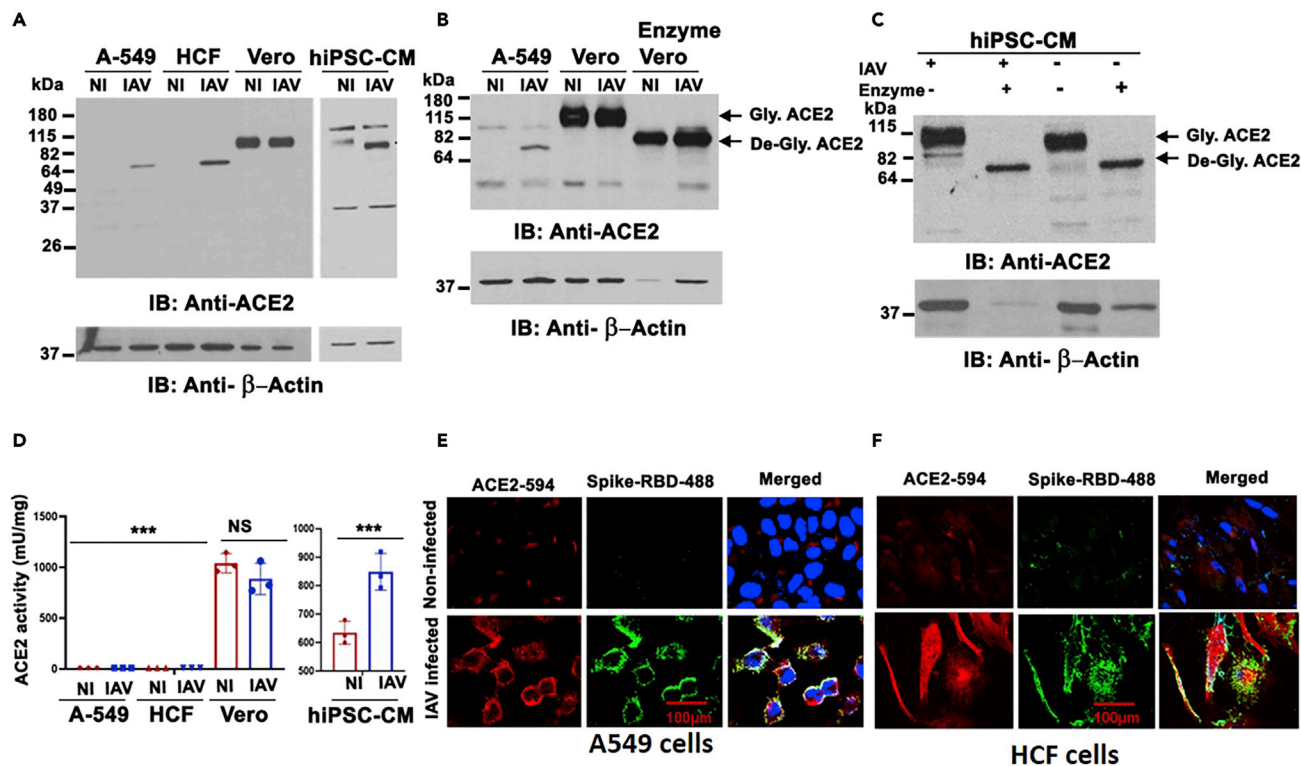
**Figure 2. IAV infection induces both glycosylated and non-glycosylated ACE2 which are able to bind to SARS-CoV-2 spike protein**

(A) To compare ACE2 protein size, cell lysates from IAV infected or uninfected A549, HCF, Vero and hiPSC-CMs were subjected to IB analysis to determine the ACE2 protein size. The blots were re-probed with β-actin antibody as loading control. Cell lysates from IAV infected and uninfected Vero cells (B) and hiPSC-CMs (C) were treated with N glucosidase, β1, 4-galactosidase, and β-N-acetylglucosaminidase or left untreated as control and subjected to IB analysis with ACE2 antibody.

(D) IAV infected and uninfected A549, HCF, Vero and hiPSC-CMs cells were lysed and the fresh cell lysates were used to determine ACE2 peptidase activity. Peptidase activity was normalized to the protein concentration. The data shown in the graph are representative of two independent experiments in which peptidase activity was measured in triplicate samples. A two-tailed Student's t test was used to analyze the data (mean $\pm$ *SEM*; \*\*\*p< 0.0005).

(E and F) Representative confocal images of A549 and HCF cells infected with IAV for 24 h or left uninfected. A549 and HCFcells were incubated with biotynylated receptor-binding domain (RDB) of SARS-CoV-2 spike protein followed by AF488 (green) conjugated streptavidin. The cells were fixed and stained with anti-ACE2 antibody followed with AF594 (red) conjugated secondary antibody. The nuclei were stained with DAPI (scale bar = 100μm).

by qRT-PCR. Our results revealed that IAV infection enhanced the expression of ACE2 mRNA in the heart (Figure 3C). To further validate the mRNA data, we examined the level of ACE2 protein expressed in heart tissue by immunoblotting with ACE2 antibody. As with the mRNA levels, the ACE2 protein level was increased by IAV infection of the heart tissue (Figure 3D). The band intensities were quantified using ImageJ software[26] (Figure 3E).

Next, to test the contribution of virus on ACE2 expression, we performed a time course of IAV infection in mice. We infected the mice with IAV and determined the ACE2 expression in the lungs (confocal microscopy) and heart (qRT-PCR) for 16 days, at 4 day intervals. Lung sections were stained with ACE2 antibody and EpCam antibody and analyzed by confocal microscopy (Figure S7A). The mean fluorescent intensity of ACE2 was measured using Image-J software and the results showed that ACE2 expression gradually increased, and peaking at day 8, and decreasing to basal level by day 16 (Figure S7B). Total RNA was extracted from the hearts of IAV-infected mice (day 0, 4, 8, 12 and 16) and used to determine the ACE2 mRNA levels by qRT-PCR. Similarly, we found that ACE2 mRNA levels increased to a maximum by day 8 and returned to the basal level by day 16 (Figure 7C). To test whether IAV induced ACE2 expression in heart tissue depends on IFN-β, we quantified IFN-β mRNA by qRT-PCR and found that IFN-β mRNA levels peaked at day 8 (severe infection) and returned to normal by day 12 (recovery) (Figure 7D). These data suggest that IAV induced IFNs may play critical role in upregulating ACE2 expression in the heart.
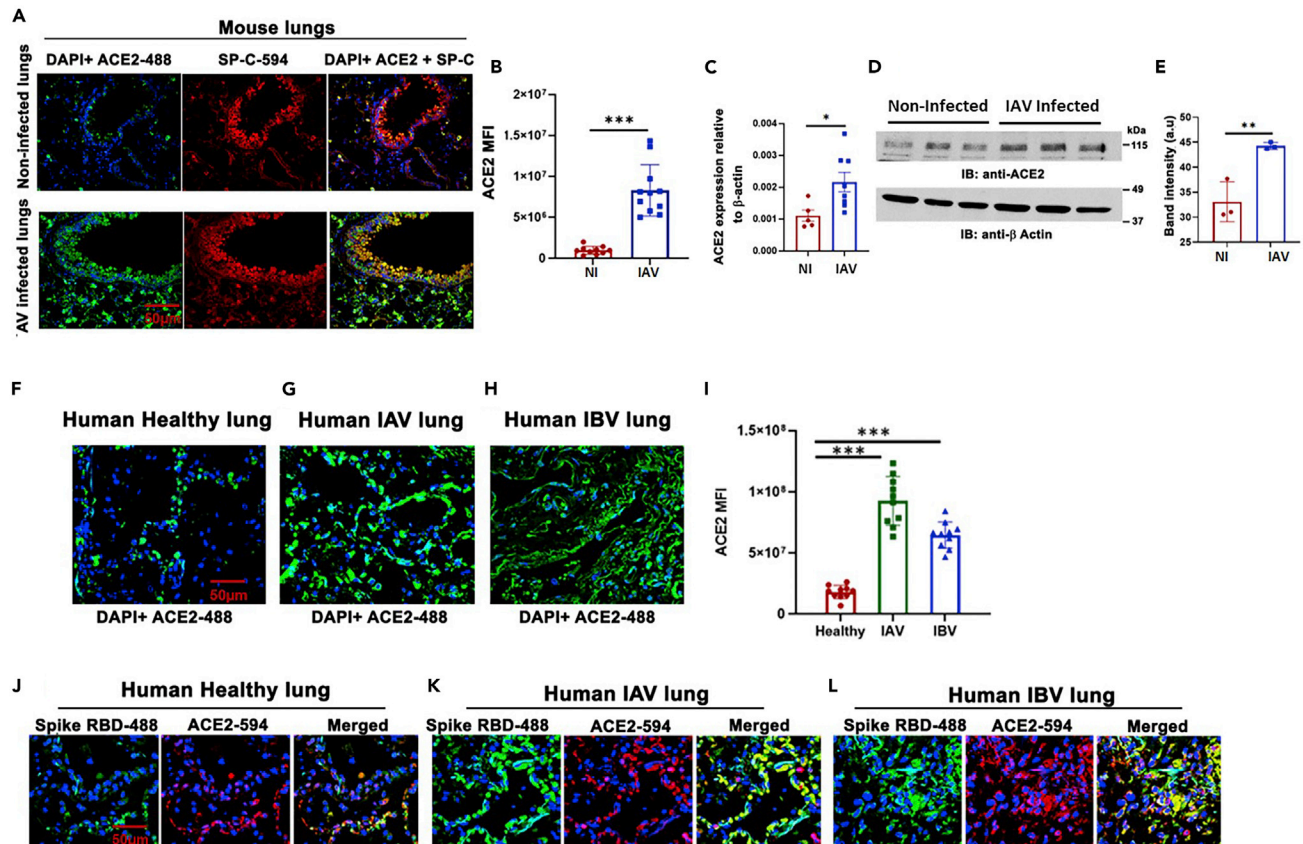
**Figure 3. IAV infection enhances the expression of ACE2 in lungs and hearts**

(A) C57BL/6 mice were infected with IAV-PR68 ($1 \times 10^4$ PFU) and on day 6 the mice were euthanized to harvest the lungs and the lungs fixed with 4% paraformaldehyde. Lung sections were stained with anti-ACE2 (Goat anti mouse; PA5-47488 from Invitrogen) and SP-C antibodies, followed by AF488 and AF594 conjugated secondary antibodies respectively. The nuclei were stained with DAPI. Confocal images (scale bar = 50μm) shown in top panel are representative images of uninfected cells and bottom panel are images of flu infected cells (n = 5).

(B) ACE2 mean fluorescent intensities from ten randomly selected images from 5 lung section were determined using ImageJ software (mean $\pm$ *SEM*; ***p< 0.0005 ;).

(C) ACE2 mRNA expression in the hearts of IAV infected mice determined by qRT-PCR using specific primers.

(D) Heart tissue from non-infected and IAV infected were lysed and the equal amount of protein was used to determine the expression of ACE2 by western blot using ACE2 specific antibody.

(E) The band intensities of ACE2 and b-actin were measured using ImajeJ software. Graph shown is band intensity normalized with beta actin (mean $\pm$ *SEM*; *p< 0.05; **p < 0.005). Human lung section from deceased non-lung disease (F), IAV infection (G) and IBV infection patients (H) were stained with anti-ACE2 antibody followed by AF480 conjugated secondary antibody and nuclei staining with DAPI (scale bar = 50μm).

(I) The ACE2 staining (green) was quantified using Photoshop CC color range selection mode. The total intensity of the stained area was further evaluated via ImageJ using color intensity. These data are cumulative from 10 different images from 3 independent experiments. A two-tailed Student's t-test was used to analyze the data (mean $\pm$ *SEM*; **p< 0.005; **p < 0.0005).

(J–L) Human lung sections from deceased patients with non-lung disease, IAV and IBV infections were incubated with biotinylated receptor-binding domain (RDB) of SARS-CoV-2 spike protein followed by AF488 conjugated streptravidin. The same slides were costained with anti- ACE2 antibody followed by AF594 conjugated secondary antibody. The nuclei were stained with DAPI (scale bar = 50μm).

Next, we examined human lung sections from deceased IAV and IBV patients and from patients whose deaths were unrelated to lung disease, stained for ACE2. Notably, similar to the mouse model, we observed increased ACE2 staining in IAV and IBV patients compared to patients who died of non-lung related diseases (Figures 3F–3H). The ACE2 fluorescent intensities of human lung sections (Figure 3I) and the accumulated data correlates well with our *in vitro* findings (Figure 1).

To determine whether IAV and IBV infection in human lungs increased binding of the spike protein, we exposed the human lung sections to spike-RBD staining and co-stained with ACE2 antibody. We found that spike-RBD binding to ACE2 was increased by influenza virus infections and that spike-RBD colocalized with ACE2 (Figures 3J and 3K and 3L and 3G).

### IAV infection enhances SARS-CoV-2 entry and replication in human lung epithelial cells and cardiac fibroblasts but inhibits the viral replication in cardio myocytes

A549, HCF, and hiPSC-CMs were infected with IAV for 48 hr and then inoculated with SARS-CoV-2 (USA-WA1/2020). SARS-CoV-2 infection and replication was examined by flow cytometry and qRT-PCR. We found that the SARS-CoV-2 infectivity is very low in uninfected A549 and HCF cells. However, prior IAV infection significantly increased the percentage of SARS-CoV-2 positive A549 (2.3% to 8.8%) and HCF cells (6.15% to 14.6%) (Figures 4A–4D), strongly supporting the concept that IAV mediated upregulation of ACE2 as observed in Figure 1 enhances the binding and entry of SARS-CoV-2. This finding was further confirmed by confocal microscopy (Figure S8). Also, a time course experiment showed that prior IAV infection favors SARS-CoV-2 replication over time in A549 and HCF cells (Figure S9). In contrast, we discovered that prior IAV infection in hiPSC-CMs significantly reduced the SARS-CoV-2 positive cells (Figures 4E and 4F). The graphs shown in Figures 4G–4L represent the cumulative data from 3 independent experiments, which confirm the increased infectivity in A549 and HCF cells and decreased infectivity in hiPSC-CMs. To further confirm our findings, we quantified SARS-CoV-2 viral replication in A549, HCF cells and hiPSC-CMs by qRT-PCR using two different primer sets to the SARS-CoV-2 N protein mRNA. Our data revealed that IAV infection significantly increased the level of N protein mRNA expression in A549 and HCF cells (Figures 4G–4J). In contrast, we observed high levels of SARS-CoV-2 N protein mRNA in hiPSC-CMs without IAV infection (Figures 4K and 4L). Unlike A549 and HCF cells, hiPSC-CMs subjected to prior infection with IAV showed substantially reduced the expression of SARS-CoV-2 N protein mRNA (Figures 4K and 4L).

Because SARS-CoV-2 is sensitive to interferons and it is known that IAV infection enhances the interferon response, we examined the levels of IFN-β in the cell culture supernatants of IAV-infected A549, HCF and hiPSC-CMs. Our data demonstrated that IAV infection enhances IFN-β production in all three different cell types, but the magnitudes of IFN-β released from hiPSC-CM is less than that from A549 or HCF cells (Figure S10). Furthermore, we tested whether different stages of IAV infection (6 h, 24 h and 48 h) alters the SARS-CoV-2 infections in these three cell types, and we observed that there is a significant increase in SARS-CoV-2 infection in A549 cells as the IAV infection progresses (Figure S11A). However, in HCF cells the SARS-CoV-2 viral replication is not changed at different stages of IAV infection (Figure S11B). In hiPSC-CMs, SARS-CoV-2 replication is significantly reduced by prior IAV infection, in all stages of IAV infection (Figure S11C).

To test whether prior IAV infection inhibits the binding or entry of SARS-CoV-2, we incubated the IAV-infected and uninfected hiPSC-CMs with SARS-CoV-2 (MOI = 20) for 2 hours and determined the % SARS-CoV-2 positive cells. Our data indicate that prior IAV infection did not affect the binding or entry of SARS-CoV-2 in hiPSC-CMs (Figure S12). To further test whether IAV infection (48h) causes contractile dysfunction or cell death in hiPSC-CMs, we monitored the hiPSC-CMs electrical activity with a multi-electrode array system. We found that IAV infection (MOI 2.5) of hiPSC-CMs did not affect the hiPSC-CMs electrical activity, contractile function and cell viability (Figure S13). These results suggest that prior infection of A549 and HCF cells with IAV makes the cells more susceptible to SARS-CoV-2 whereas prior IAV infection of hiPSC-CM cells renders the cells more resistant to SARS-CoV-2 replication.

### IAV infection differentially regulates the expression of genes in HCF and hiPSC-CMs

Because we found that prior IAV infection enhances SARS-CoV-2 replication in HCF cells and restricts it in hiPSC-CMs, we performed total RNA sequencing of IAV-infected HCF and hiPSC-CMs and compared their gene expression patterns at 48 h post infection, using a cutoff of p-value <0.001 for statistical significance. The heat map in Figure 5A and volcano plot in Figure 5B show the pattern of differentially expressed genes in hiPSC-CMs. Of the 2808 differentially expressed genes, the IFN response genes such as ISG15, ISG20, IFITM1, IFITM2, IFITM3 IRF2, IRF7 and IFNB1 were downregulated at 48 h in hiPSC-CMs. IFNRL1 was upregulated in hiPSC-CMs compared to HCF cells (Figure S14A), whereas expression of the inflammatory cytokines, TNF, IL6, IL1β, IL24 and IL12A, are significantly increased in HCF cells (Figure S14B). Because we had found increased expression of glycosylated ACE2 in hiPSC-CMs, we examined the expression of genes involved in glycosylation in our RNA sequencing data set. Expression of several N-acetylglucosaminyltransferases (MGAT4A/GNTIV, MGAT3/GNTIII, MGAT2/GNTII and MGAT5/GNTV) were highly induced in hiPSC-CMs (Figure 5C). We confirmed the gene expression profiling results from total RNA sequencing with qRT-PCR for important upregulated glycosylation genes (MGAT3 and
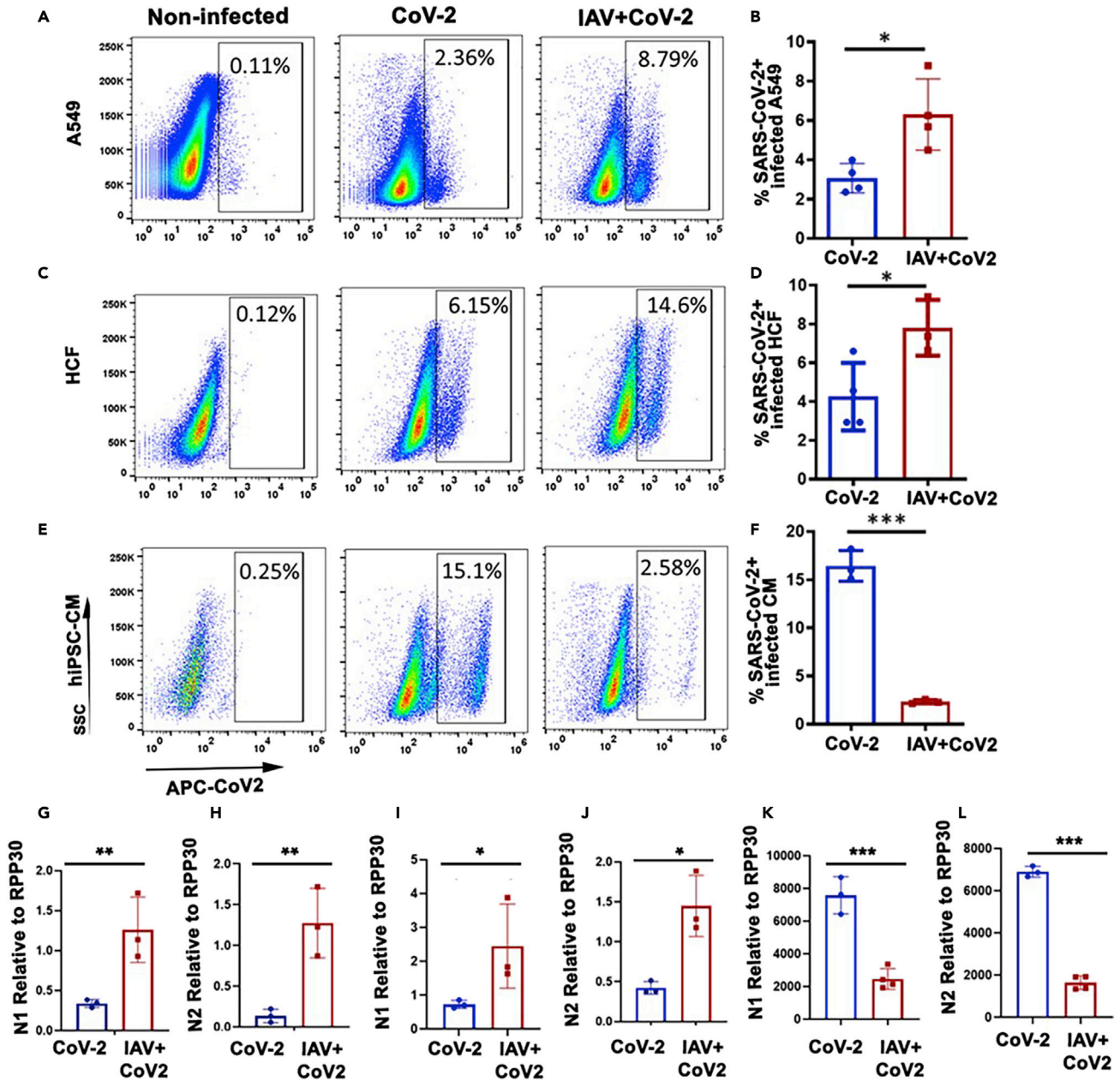
**Figure 4. IAV infection enhances the SARS-CoV-2 infectivity**

(A–F) A549, HCF and hiPSC-CMs cells were infected with IAV or left uninfected for 48 h, washed and exposed with SARS-CoV-2 (MOI 2). After 24 h, cells were harvested to analyze the SARS-COV2 infectivity by flow cytometry or qRT-PCR. Flow cytometry plots of uninfected, SARS-CoV-2 only and IAV + SARS-CoV-2 of A549 (A), HCF (C) and hiPSC-CMs (E) demonstrate enhanced SARS-CoV-2 infectivity in IAV infected cells. Graphs shown in (B), (D) and (F) are representative of SARS-CoV-2 positive cells calculated from the flow data obtained from three independent experiments in quadruplicate samples. A two-tailed Student's t-test was used to analyze the data (mean $\pm$ SEM; *p< 0.05; **p< 0.005).

(G–L) Graphs shown in G–L are relative mRNA expression of the SARS-CoV-2 N protein in A549 (G, H), HCF (I, J) and hiPSC-CMs (K, L) infected with SARS-CoV-2 only or IAV + SARS-CoV-2. mRNA expression was determined by qRT-PCR using N1 and N2 primers and expressed relative to the house-keeping gene Rpp30. Data shown area representative of three independent experiments performed in triplicate or quadruplicates. A two-tailed Student's t-test was used to analyze the data (mean $\pm$ SEM; *p< 0.05; **p < 0.005; ***p< 0.0005).

MGAT4A) in IAV-infected HCF and hiPSC-CMs (Figures 5D and 5E). Taken together these results strongly indicate that IAV infection induces both the interferon and inflammatory gene response in HCF cells, suggesting that these cells are more susceptible to infection than hiPSC-CMs.
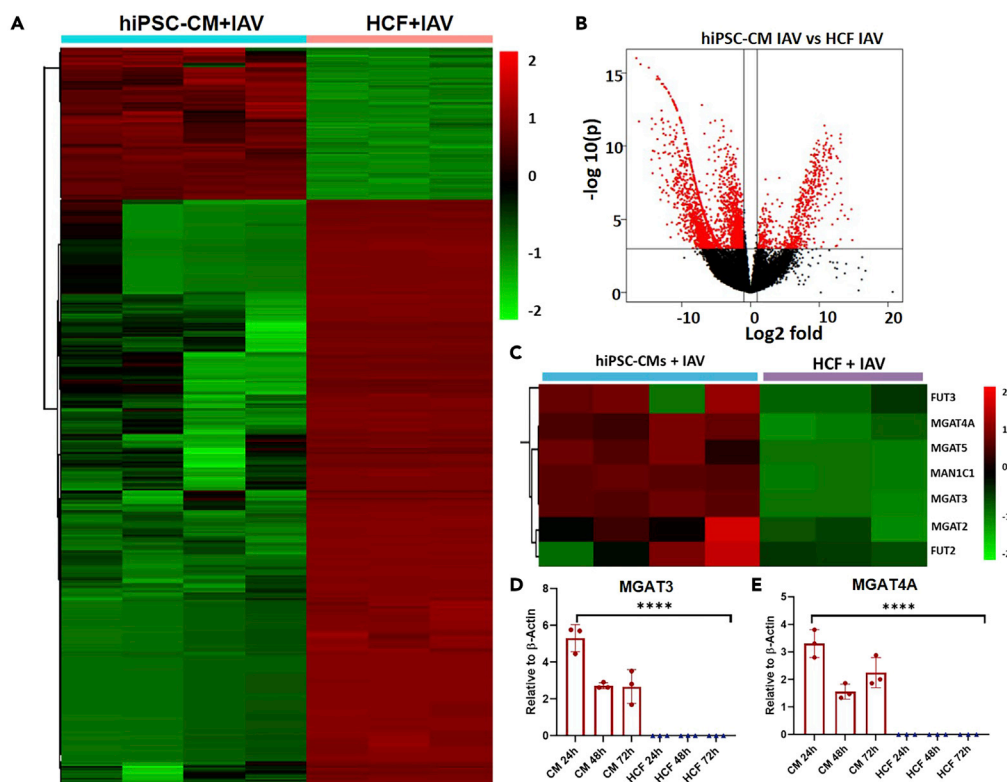
**Figure 5. IAV infection differentially regulate the gene expression in HCF cells and hiPSC-CMs**
Comparative analysis of differentially expressed genes in IAV infected HCF and hiPSC-CMs.
(A) Heatmap.
(B) Volcano blot showing the differential gene expression in IAV infected HCF and hiPSC-CMs.
(C) Selected glucosamilytransferase gene expression of IAV infected HCF and hi-PSC-CMs.
(D) Validation of MGAT3.
(E) MGAT4A by qRT-PCR. Data shown in graphs are a representative of three experiments. A two-tailed Student's t-test was used to analyze the data (mean $\pm$ SEM; ***p< 0.0005).

## Heat killed SARS-CoV-2 cause's arrhythmia in hiPSC-CM cells

Previous studies have found that SARS-CoV-2 infection of hiPSC-CMs causes cardiomyocyte contractile dysfunction[27,28] and our results show that hiPSC-CMs are permissive for SARS-CoV-2 infection (Figure 4). That finding prompted us to investigate the impact of SARS-CoV-2 on cardiomyocyte contractile function, field potential and spike amplitude using a multi-electrode array system. Because we could not employ this system in the BSL3 laboratory, we instead exposed the hiPSC-CMs to heat-killed SARS-CoV-2 at an MOI of 1 and 2.5 and recorded the cardiomyocyte electrical functions over time (0–24 hours). Incubation of heat killed SARS-CoV-2 with hiPSC-CMs significantly increased the cardiomyocyte beat rate (Figures 6A and 6B) and decreased the beat period at 6 h (Figures 6A and 6B). Furthermore, the field potential duration (FPD) in heat killed SARS-CoV-2-exposed hiPSC-CMs was also decreased (Figure 6C). FPD represents the characteristics of action potential (AP) and QT interval of the ECG.[29,30] The shortening of FPD shows altered action potential (AP) and ultimately indicates ion channel imbalance and the presence of arrhythmias. However, the hiPSC-CM response to HK SARS-CoV-2 was transient and returned to normal contractility within 24 h of HK SARS-Co-V-2 incubation (Figure S15), which suggests that live virus replication is required for the induction of long-term cardiomyocyte contractile dysfunction as has been reported.[31]

Next, we tested whether the interaction of spike protein with ACE2 is enough to induce the cardiomyocyte contractile dysfunction. The hiPSC-CMs were incubated with recombinant spike protein or spike receptor binding domain (RDB) and the cells were monitored for cardiomyocyte function. Of interest, we found that the incubation of spike protein or its RDB did not cause any abnormalities of cardiomyocyte contractile
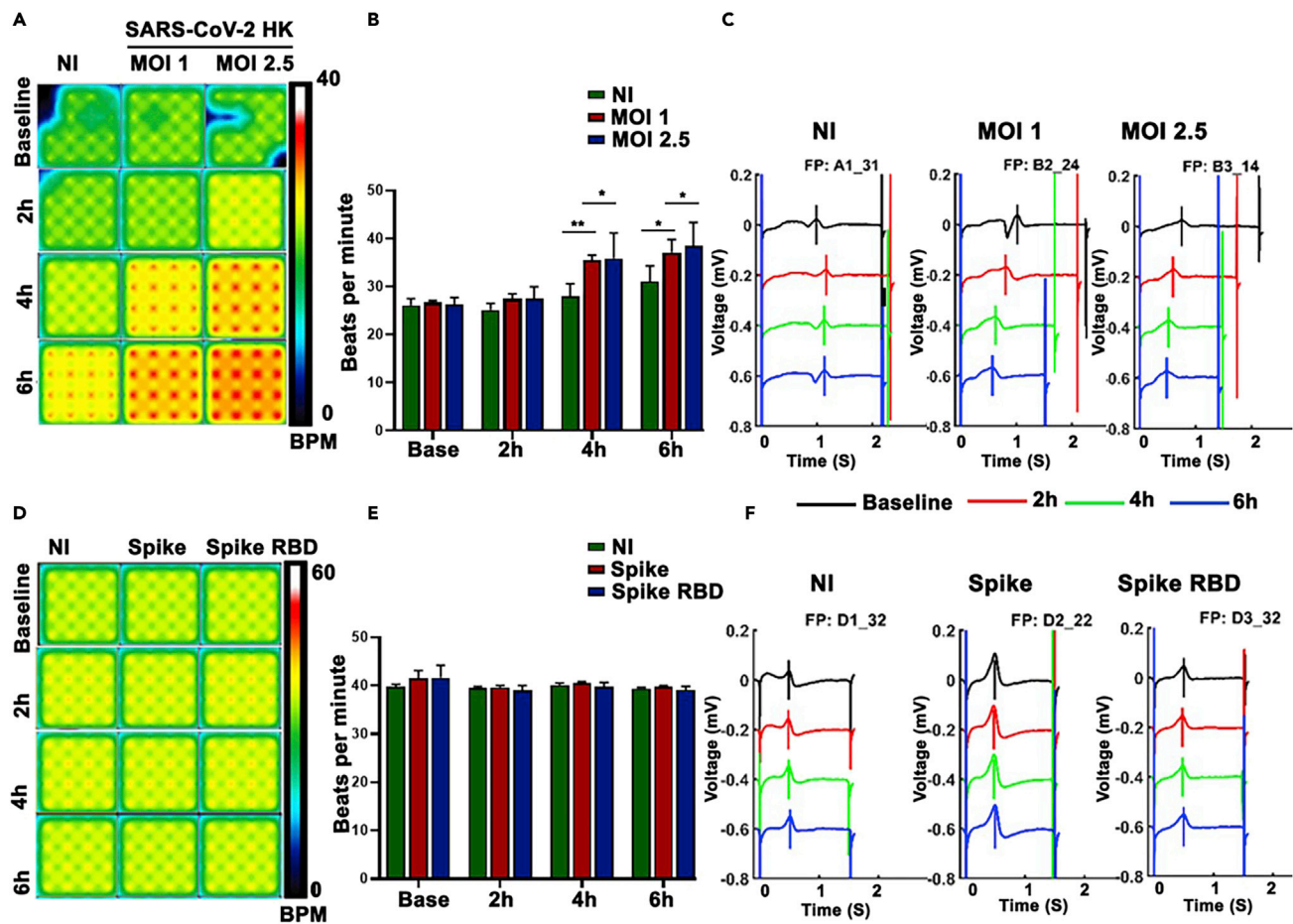
**Figure 6. SARS-CoV-2 causes cardiomyocyte contractile dysfunction**

hiPSC-CMs ($3.5 \times 10^4$ cells/well) were plated in 24 well MEA plates and the cells were left untreated or treated with heat killed (HK) SARS-CoV-2 at a MOI 1 and MOI 2.5 (A) or recombinant spike protein and spike receptor binding domain (RDB) (D). The cardiomyocyte contractility and electrical activity was recorded using AxIS Navigator on the MEA system at 5% $CO_2$ and at 37 °C for indicated time points. Data analysis was performed using the cardiac analysis tool.

(A and D) Activity map showing changes in beat rate of cardiomyocytes treated with HK SARS-CoV-2 and spike proteins. Shown is a representative well from quadruplicate samples for each treatment (N = 2).

(B and E) The graphs shown in B and E are the number of cardiomyocyte beats per minute at baseline and at 2, 4 and 6h post treatment. Data shown is a representative of two independent experiments performed in quadruplicate wells. A two-tailed Student's t-test was used to analyze the data (mean $\pm$ *SEM*; *p< 0.05; **p< 0.005).

(C and F) Representative traces recorded with the MEA system showing the beat period, T-wave and FPD in untreated control, HK SARS-CoV-2 (MOI 1 and MOI 2), spike protein and spike RDB treated cardiomyocytes.

function: there was no difference in beat period and FPD, and the electrocardiogram traces were not different from the control without spike protein (Figures 6D–6F). Together, these data indicate that the interaction of spike protein with the receptor ACE2 is not enough to cause cardiomyocyte contractile dysfunction, suggesting that the effects on contractions require infection or at least live virus.

## IAV infection increases the level of angiotensin II in A549 and HCF cells

ACE2 is a carboxypeptidase that converts the Ang II into angiotensin1-7 and thereby inhibiting the Ang II-mediated pro-inflammatory response.[32] We found that IAV infection mediated upregulation of ACE2 expression in A549 and HCF cells but there was no apparent increase in peptidase activity. In contrast, IAV infection of hiPSC CMs increases the ACE2 expression and peptidase activity (Figure 2D). These observations prompted us to look for evidence of peptidase activity by measuring the level of Ang II in the culture supernatants harvested from uninfected vs IAV-infected A549, HCF and hiPSC-CMs. Notably, we found that the Ang II levels were significantly increased in cultures of IAV-infected A549 and HCF cells
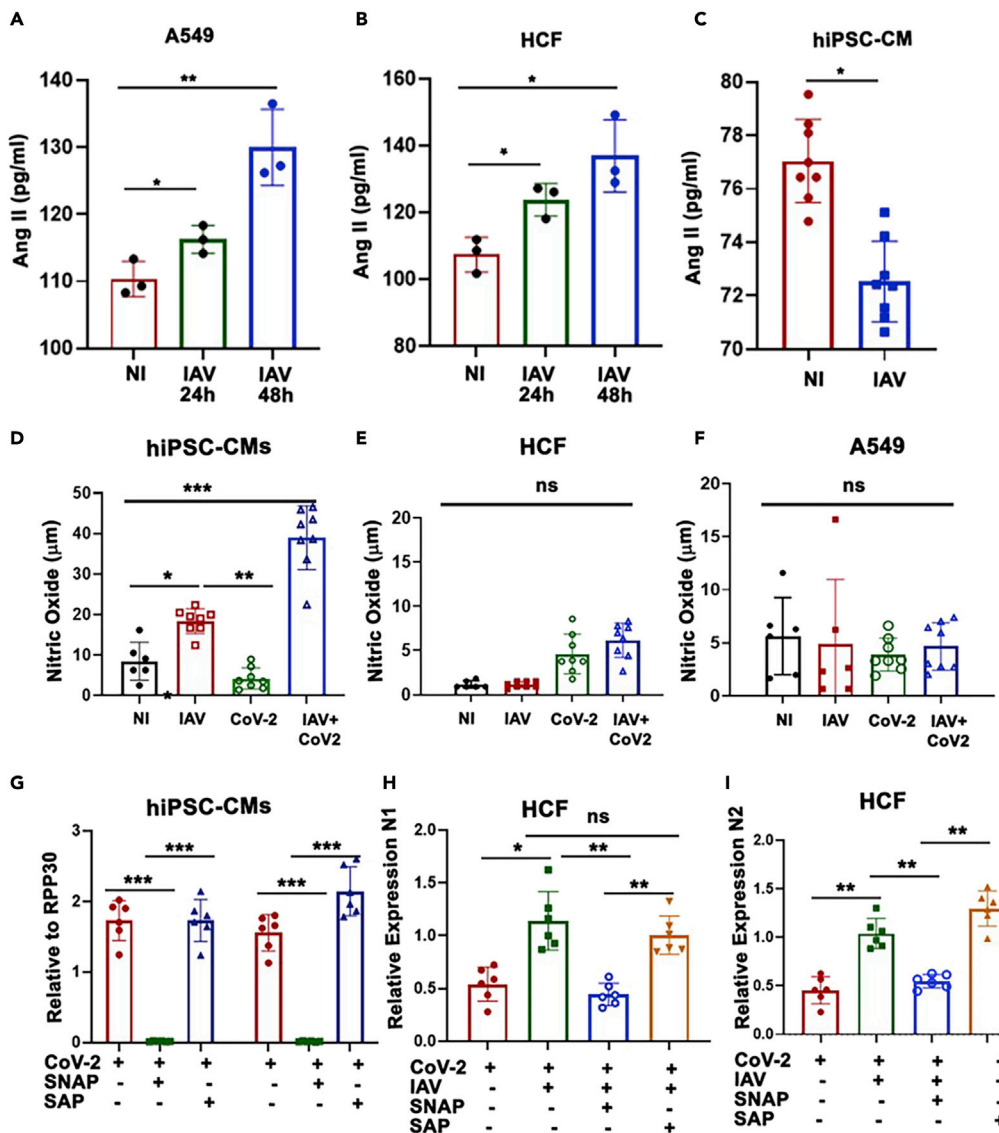
**Figure 7. IAV infection promotes renin angiotensin system and restricts the SARS-CoV-2 replication**

(A) A549, (B) HCF and (C) hiPSC-CMs were infected with IAV or left uninfected for 48 h. The cell free culture supernatants were harvested and the Ang II levels determined by ELISA (A–C), and the nitrite production assessed by measurement of nitrite ($NO_2^-$) using Griess reagent (D–F).

(G) hiPSC-CMs were directly infected with SARS-CoV-2 (MOI 2) and aafter an hour of incubation the cells were exposed to media only, SNAP (400μM ) and NAP (400μM) for 24 hours.

(H and I) HCF cells were infected with IAV or left uninfected for 48hs, washed and incubated with SARS-CoV-2 (MOI 2) and after one hour the cells were treated with media only, SNAP (400μM ) and NAP (400μM) for 24 hours. The cells were lysed and total RNA was used to determine the relative mRNA expression of SARS-CoV-2 N gene by qRT-PCR using N1 and N2 primers and expressed relative to the house-keeping gene Rpp30. Data shown in graph A-C are representative of three independent experiments performed in triplicate or quadruplicates. A two-tailed Student's t-test was used to analyze the data (mean ± SEM; *p< 0.05; **p< 0.005). Data shown are representative of three independent experiments performed in triplicate or quadruplicates. A two-tailed Student's t-test was used to analyze the data (mean ± SEM; ns-nonsignificant; *p< 0.05; **p< 0.005; ***p< 0.0005).

indicating that these cells produce Ang II but lack the ACE2 enzymatic activity to convert it to Ang 1–7 (Figures 7A and 7B). However, the IAV infection significantly reduced the levels of Ang II in hiPSC-CMs (Figure 7C). Together, our results demonstrated that the IAV mediated induction of highly glycosylated ACE2 expression in hiPSC-CMs activates it enzymatic activity (Figures 2C and 2D), converting the

proinflamamtory Ang II into immunosuppressive Ang 1–7, paving the way for a secondary infection by SARS-CoV-2 in an immunosuppressed environment.

### Prior IAV infection enhances the production of nitric oxide in hiPSC-CMs, but not in A549 and HCF cells

It has been previously reported that the conversion of Ang II to Ang 1–7 and the binding of Ang 1–7 to the Mas receptor leads to the activation of the PI3K/Akt pathway resulting in upregulation of NOS3 (eNOS) and the production of $NO_2^{-}$[33] To determine if this pathway has been activated, we measured eNOS (NOS3) expression in HCF and hiPSC-CMs, and we found that eNOS expression is not induced in HCF cells by either CoV-2 alone or IAV with CoV-2, but we observed an significant increase in eNOS expression in hiPSC-CMs on CoV-2 and IA with CoV-2 (Figure S16). Next, we measured the $NO_2^{-}$ in in cell culture supernatants of A549, HCF and hiPSC-CMs. As expected from experiments above, prior IAV infection of hiPSC-CMs increased $NO_2^{-}$ levels in culture supernatants because of reduced levels of AngII, but infection of HCF and A549 cells did not, because of high levels of Ang II (Figures 7D–7F). $NO_2^{-}$ has been found to inhibit SARS-CoV-2 replication[34] which might explain why prior infection with IAV inhibits SARS-CoV-2 replication in hiPSC-CMs but not in A549 or HCF. To confirm that the induction of $NO_2^{-}$ production inhibits the replication of SARS-CoV-2, we treated SARS-CoV-2-infected hiPSC-CMs (susceptible to SARS-CoV-2 without prior IAV infection) with S-nitroso-N-acetyl-DL-penicillamine (SNAP) ($NO_2^{-}$ donor) or N-acetyl-DL-penicillamine (NAP) (control), and measured N protein mRNA levels after 24 h. SNAP treatment diminished the SARS-CoV-2 replication in hiPSC-CMs (Figures 7G and 7D). Because the hiPSC-CMs are metabolically active and the $NO_2^{-}$ might induce contractile dysfunction and cell death, we exposed hiPSC-CMs to SNAP or NAP and monitored their contractile function with the MEA system and cytotoxicity with the LDH assay. The MEA data (Figures S17A and S17B) revealed that SNAP increased the beats per minute immediately after adding, however the beat frequency returned to normal within 3 h. Furthermore, the cell morphology did not change over this time and LDH was not released (cell death) indicating that $NO_2^{-}$ is not toxic for hiPSC-CMs (Figure S17C).

Because we found that prior IAV infection enhances SARS-CoV-2 infectivity of HCF cells, we determined if SNAP treatment inhibited the SARS-CoV-2 replication in HCF cells that were infected with IAV + SARS-CoV-2. After 24 h, total RNA was extracted, and SARS-CoV-2 N protein mRNA expression was determined. We found that the addition of SNAP significantly reduced SARS-CoV-2 replication in HCF cells as measured the N protein mRNA levels (Figures 7H and 7I). To determine whether SNAP was producing $NO_2^{-}$ in HCF cells, we infected HCF cells with IAV and, after a 24 h treatment with or without SNAP and NAP, measured $NO^{-}_2$ in the supernatant. SNAP treatment increased the production of $NO_2^{-}$ in HCF cells (Figure S18). Together, our results revealed that $NO^{-}_2$ plays an important role in inhibiting the SARS-CoV-2 replication for both hiPSC-MCs and HCF.

### Prior IAV infection enhances the mortality of SARS-CoV-2 infected mice

To study the interaction between IAV and SARS-CoV-2 *in vivo*, we infected C57BL/6 mice with $1 \times 10^5$ PFU of mouse adapted SARS-CoV-2 strain MA10 with or without a 5-day prior infection with IAV strain PR8 ($1 \times 10^4$ PFU) and monitored the morbidity and mortality through day 12. The survival rate of the mice (Figure 8A) and our results revealed that prior IAV infection increases the mortality of SARS-CoV-2 co-infected mice (90% of the mice were dead by day 12). In contrast, only 30% of mice infected with SARS-CoV-2 alone died by day 12. Next, we determined the virus titers in the lung and heart homogenates of the mice that survived SARS-CoV-2, alone, and IAV with SARS-CoV-2. We found an increase of SARS-CoV-2 titer in the lungs and hearts of IAV-infected mice (only 2 out of 15 mice survived), compared to SARS-CoV-2, alone, infected mice (Figures 8B and 8C). Taken together, these data are consistent with prior IAV infection enhancing the expression of ACE2 in the lungs and hearts and promoting SARS-CoV-2 entry and replication.

## DISCUSSION

The current study revealed several novel findings. First, we determined that IAV infection resulted in elevated expression of the SARS-CoV-2 receptor, ACE2, but not the cofactor TMPRSS2 in all three human cell types studied, A549, HCF and hiPSC-CMs. Furthermore, we determined that ACE2 glycosylation correlated with ACE2 peptidase activity, which facilitates the conversion of pro-inflamamtory Ang II to immunosuppressive Ang 1–7, and thereby increasing the expression of NOS3 and $NO_2^{-}$ production. Of
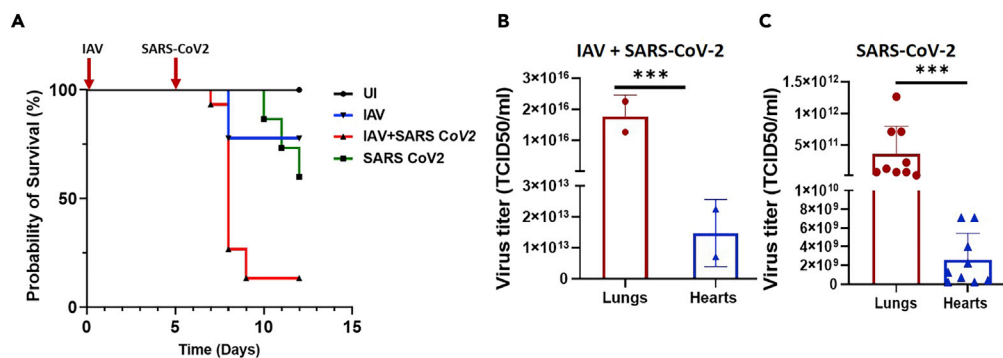
**Figure 8. Prior IAV infection increases SARS-CoV-2 virus replication and mortality in mice**

C57BL/6 (8-10-week old) mice were intranasally infected with IAV strain PR8 ($1 \times 10^4$ PFU) in sterile saline. After 5 days, the influenza A virus-infected mice and uninfected mice were intranasally infected with mouse adapted SARS-CoV-2 strain MA10 ($1 \times 10^5$ PFU).

(A–C) Survival of the mice were monitored until day 12 (n = 15 per group) (A), lungs and heart tissues were collected, homogenized, and used to determine the TCID50 virus titer assays on Vero E6 cells using 10-fold serial dilutions assayed in triplicate. The presence of virus replication in each well was assessed by visual examination of cytopathic effect with antibody staining for SARS-CoV-2 N protein antigen (mouse mAb 40143-MM08, Sino Biological) with fluorescent secondary antibody detection. TCID50 titers were calculated using the Reed-Muench method. Viral titers in lung (B) and heart (C) homogenates of IAV_SARS-CoV-2 and SARS-CoV-2 alone mice were measured using TCID titers. A two-tailed Student's t-test was used to analyze the data (mean ± *SEM*; ns-nonsignificant; ***p< 0.0005).

interest, IAV induced glycosylation differs between human lung epithelial cells, cardiac fibroblasts, and cardiomyocytes and thereby differentially influences the outcome of the SARS-CoV-2 infection.

Infection with IAV induced the expression of ACE2 in A549, HCF, hMDMs and hiPSC-CMs. Of interest, the molecular weight of IAV-induced ACE2 in A549, HCF cells and human MDMs is only ∼72 kDa, whereas it is 115 kDa in hiPSC-CM (Figure 1). The fact that the molecular weight of ACE2 in A549 and HCF cells is less than the predicated molecular weight of non-glycosylated ACE2 (85 kDa) has been suggested to be due to cleavage of ACE2 at a site in the C-terminal region by TMPRSS2 which is induced in these cells by IAV infection.[35] Of interest, the cleaved ACE2 is retained by the cell and promotes entry of the SARS-CoV-2 virus. The size of the C-terminal fragment is 13 kDa. Thus, the 72 kDa ACE2 in IAV-infected cells (A549 and HCF) is the cleaved ACE2 fragment which contains the transmembrane domain (Figure 1). Studies from Onabajo et al., identified an ACE2 isoform that is an interferon and virus induced gene product; specifically, a truncated isoform of ACE2, designated as delta ACE2, which lacks 356 amino-terminal amino acids therefore its non-functional in binding the SARS-CoV-2 [22]. Similarly, Ng et al., also demonstrated that a truncated ACE2 transcript is induced in response to IFNs, termed *MIRb-ACE2*, but it is unstable and would not be translated into protein.[23] These studies reported that dACE2, but not ACE2 is induced by IFNs and viruses. In contrast, our IB analysis of human primary cells and cell lines showed an increased ACE2 expression (Figure 1) which indicated that IAV induces the expression of the full-length ACE2. Notably, the antibody used to detect ACE2 in our system is raised against an epitope in the N-terminal region of ACE2 and does not detect dACE2. This conclusion is supported by experiments with IAV infection in A549 and HCF cells in which qRT-PCR analysis revealed that IAV infection induces the expression of both full and dACE2 forms (Figures S2A–S2D). Our findings of IAV mediated upregulation of ACE2 in cell lines was also supported by *in vivo* mouse and human infections (Figure 3) and supported by Bai et al.[11]

ACE2 expression is regulated transcriptionally and post-transcriptionally and involves an epigenetic process. The has-miR-125a-5p and miR200 families of microRNA are known to target the 3′UTR of the ACE2 mRNA and regulate ACE2 expression at the post-transcriptional level.[36] The ACE2 promoter has proximal and distal regulatory regions and the relative use of the two promoter components varies among the tissues.[37] Chromatin immunoprecipitation sequencing (ChIP-Seq) studies have revealed that ACE2 gene expression is regulated by several transcriptional factors including MYBL2, USF1, TAED4, EP300, SP1, HNF4A, CEBP, MAFF and GATA3.[38] Furthermore, Kuan et al demonstrated that angiotensin II induces the expression of ACE2 in human cardiac fibroblasts.[39] We have found that the Ang II level is high in IAV-infected A549, HCF and hiPSC-CMS (Figure 8). Also, several studies demonstrated that ACE2 is an IFN stimulated gene and the transcription factors STAT1, STAT3, IRF8 and IRF1 bind to the ACE2 promoter

region,[40,41] suggesting ACE2 induction in these cells. Further detailed studies are required to identify the exact mechanism and transcription factors involved in the induction of ACE2 on IAV infection. The host immune cells respond to IAV infection by producing type I and III IFNs. The released IFN binds to its receptor and induces various IFN response genes, which provide a first line of defense against IAV and encounters with the invading virus.[42] ACE2 has been described as an interferon response gene in human airway epithelial cells and other cell types in the body.[40]

Studies from Shajahan et al., have shown that human ACE2 contains seven N-glycosylation sites and one O-glycosylation site,[19] and the glycosylation of ACE2 is essential for it peptidase activity.[43] Remarkably, we observed that the IAV-induced ACE2 in A549 and HCF cells is not glycosylated; whereas IAV-induced ACE2 in hiPSC-CMs is glycosylated (Figures 2A–2C) and exhibits peptidase activity[43] (Figure 2D). Furthermore, our data showed that IAV-induced ACE2 is able to bind the spike protein in A549 and HCF cells (Figures 2E and 2F), which suggests that the 72 kDa non-glycosylated ACE2 is capable of engaging the spike protein on SARS-CoV-2. Because enhanced binding of spike protein to IAV-infected cells does not necessarily lead to enhanced pathogenicity of a SARS-CoV-2 infection, we were prompted to determine whether IAV-induced ACE2 expression enhances SARS-CoV-2 infectivity in these cells. Therefore, we inoculated IAV-infected A549, HCF and hiPSC-CMs with SARS-CoV-2 and monitored its replication and infectivity. Consistent with a recent report from Bai et al.[11], we observed increased infectivity in A549 and HCF cells pre-infected with IAV. By contrast, we observed that in hiPSC-CMs, IAV pre-infection significantly diminished the SARS-CoV-2 replication, without affecting the entry of SARS-CoV-2 (Figures 4 and S6). However, we found that the ACE2 induced in hiPSC-CMs by IAV that was highly glycosylated and showed peptidase activity, whereas the ACE2 induced in A549 and HCF cells by IAV infection was non-glycosylated and lacked peptidase activity (Figures 1 and 2).

Importantly, in this manuscript we showed that exposure of hiPSC-CMs to heat killed SARS-CoV-2 significantly increased cardiomyocyte contractility and shortened the T wave (Figure 7). However, incubation of spike protein and spike RDB with hiPSC-CMs did not affect CM contractile function, suggesting that the interaction of spike protein with ACE2 is not involved in the dysregulation of cardiomyocyte function. We speculate that SARS-CoV-2 replication is required for the induction of the CM contractile dysfunction. Consistent with our studies, Yang et al., demonstrated that hiPSC-CMs express ACE2 that enables the entry of SARS-CoV-2 pseudo virus.[27] Similarly, Sharma et al., demonstrated that hiPSC-CMs are susceptible to SARS-CoV-2 infection, and on infection activate genes for antiviral responses while suppressing those involved in cardiomyocyte contractility, which collectively leads to cardiomyocyte contractile dysfunction.[44] Therefore, these cells provide a valuable model to study cardiac dysfunction during SARS-CoV-2 infection.

ACE2-catalyzed conversion of Ang II into Ang (1–7) and the consequent anti-inflammatory effects have been well established.[17,18] Remarkably, we observed an increased level of Ang II in IAV-infected A549 and HCF cells. In contrast, the level of Ang II in hiPSC-CMs was significantly reduced (Figure 7), suggesting that increased expression and glycosylation of ACE2 in hiPSC-CMs exhibits an increased enzymatic activity that converts Ang II into Ang (1–7). Binding of Ang (1–7) to MasR activates the PI3K/Akt signaling pathway to induce the expression of eNOS.[45] Also, Ang (1–7) has been shown to function protectively in the heart during ischemic injury by enhancing the function of endothelial cells, vasodilation, expression of SERCA2, NOS3 and $NO_2^-$.[33] Notably, we observed elevated levels of $NO_2^-$ in hiPSC-CMs (Figures 7D–7F), which correlated with the decreased SARS-CoV-2 viral load in IAV + SARS-CoV-2 co-infected cells (Figure 5). It had been shown previously that SARS-CoV-2 is sensitive to interferons[46] and IAV infection is known to induce an interferon response, thus it is possible that IAV-induced IFN is responsible for the inhibition of SARS-CoV-2 replication in hiPSC-CMs. However, we found similar levels of IFN-β in A549, HCF and hiPSC-CM cells infected with IAV (Figure S10), yet we found a significant decrease in SARS-CoV-2 replication/load in CMs, which suggests that the suppression of SARS-CoV-2 replication in hiPSC-CM cells is independent of IAV-induced IFNs. Collectively, our data revealed that the control of SARS-CoV-2 in hiPSC-CMs previously infected with IAV is because of increased expression of NOS3 and $NO_2^-$ production. In contrast, in A549 and HCF cells, co-infection with IAV and SARS-CoV-2 failed to increase NOS3 expression and $NO_2^-$ production and thereby failed to control SARS-CoV-2 replication. Nitric oxide has a broad-range antimicrobial effect against various pathogens including both DNA and RNA viruses.[47–50] Likewise, and similar to our results, the SNAP-mediated inhibition of SARS-CoV-2 replication was also reported by Akaberi et al.[34] Notably, our findings revealed that an increased state of glycosylation and NO production in hiPSC-CMs enhanced the inhibition of IAV replication in our co-infection model (Figures 1C, 2C, 2D,

and 8). In contrast, the increased expression of non-glycosylated ACE2 in A549 and HCF cells enhances the replication of SARS-CoV-2, which may be because of the lack of ACE2 enzymatic activity and $NO_2^-$ production (Figures 1A, 1B, 2D, and 8). Furthermore, our mouse co-infection studies revealed that prior IAV infection enhances the presence of SARS-CoV-2 in the lung and heart and subsequently increases the mortality (Figure 8). Although, we predicted that prior IAV infection may protect the heart from virus replication, because of the expression of glycosylated ACE2 and its enzymatic activity, we found increased virus titers in the hearts. The reasons for the increased virus titer in the heart could be the cellular composition of the heart and induction of unglycosylated ACE2 in cardiac fibroblasts, further work is needed to determine the cell type infected by SARS-CoV-2 in the heart. Our results are strongly supported by clinical data from COVID-19 patients with flu-like symptoms demonstrating the presence of SARS-CoV-2 in the heart tissue but not specifically in the cardiomyocytes.[51] A multi-organ autopsy study by Puelles et al., also showed the presence of SARS-CoV-2 viral particles in heart tissue.[52] However, the cell type harboring the virus was not identified. It is important to note that we tested whether inhibition of glycosylation by tunicamycin enhanced the infectivity of SARS-CoV-2 in hiPSC-CMs and Vero-E6 cells. Surprisingly, we found that treatment with a glycosylation inhibitor (tunicamycin) significantly reduced SARS-CoV-2 replication, which may be due to the inhibition of glycosylation of the viral glycoproteins (data not shown). Thus, our studies suggest that cardiomyocytes are susceptible to SARS-CoV-2 infection and that co-infection with IAV primes these cells by inducing the expression of IFN response genes including ACE2 and its glycosylation, which may protect cardiomyocytes from SARS-CoV-2.

In summary, we showed that lung epithelial cells and cardiac fibroblast succumb to SARS-CoV-2 when pre-infected with IAV; whereas, cardiomyocytes are resistant to SARS-CoV-2 infection. The cardiomyocytes offer protection by way of upregulating the expression of glycosylated forms of ACE2 and subsequent up-regulation of nitric oxide. We hypothesize that nitric oxide upregulation by hiPSC-CMs should help control SARS-CoV-2 infection in the local cardiac microenvironment, which includes other heart cells. Co-infection of SARS-CoV-2 and IAV enhances SARS-CoV-2 infection *in vivo* in human ACE2 transgenic mice,[11] concurring with our *in vitro* findings.

Our data suggest that the heart, but not the lung, may be protected during SARS-CoV-2 infection by a previous infection of IAV. It is plausible that flu vaccine may offer cardio protection by enhancing the glycosylated ACE2 expression and also protect the lungs by enhancing the IFN response which controls the SARS-CoV2 pathogenesis in the lungs. However, flu vaccine may give an opportunity to concentrate and treat lung infection in COVID-19 patients, without worrying about a cardiac dysfunction or in patients with preexisting cardiovascular conditions. Importantly, pharmacological agents that specifically enhance ACE2 protein glycosylation and NO donors might be targets for treating lung infections with IAV and SARS-CoV-2.

### Limitations of the study

Though our study identifies the basic mechanism of how IAV co-infection restricts SARS-CoV2 replication in hiPSC-CMs by enhancing the glycosylation of ACE2 and its downstream activation of NO production, the role of glycosylated ACE2 on SARS-CoV2 pathogenesis is not clearly identified. Our RNA sequencing data revealed that IAV infection induces the expression of several N –glycosylation genes (MGAT3 and MGAT4A, etc.) in cardiomyocytes only (Figure 5). To test whether these glycosylation genes are responsible for the glycosylation of ACE2 in cardiomyocytes, we will knockdown these specific genes (MGAT3 and MGAT4A etc.) in hiPSCs and differentiate them into hiPSC-CMs and study their role in IAV + SARS-CoV-2 infectivity. Furthermore, the current manuscript does not address the cells that harbor SARS-CoV2 in IAV co-infected animal hearts. To identify the cell types, we will stain the heart sections with cell specific markers with SARS-CoV2 NP antibody. Although, we have shown that other viral strains such as IBV and MPV, induces ACE2 expression, our studies are limited to PR8 influenza strain rather than the contemporary IAV strains such as H1N1, H3N2 etc. Thus, additional experiments and further investigation are ongoing to clearly dissect the mechanism of IAV mediated SARS-CoV2 pathogenesis.

### STAR★METHODS

Detailed methods are provided in the online version of this paper and include the following:

- KEY RESOURCES TABLE
- RESOURCE AVAILABILITY
  - Lead contact

## SUPPLEMENTAL INFORMATION

Supplemental information can be found online at https://doi.org/10.1016/j.isci.2022.105701.

## AUTHOR CONTRIBUTIONS

Authors Q.W., W.L.P., and N.K. contributed equally. Q.W., W.L.P., N.K., O.S.A., E.W., N.S.E., M.E.R., A.Z., M.K.C., L.P.G., and M.V.S.R. performed the experiments, analyzed data, and generated figures. J.S.Y. and

M.E.P. provided assistance and expertise in IAV and SARS-CoV-2 strains for infection in BSL2 and BSL3 facilities. A.K.P. provided human lung sections and data analysis. Experiments were supervised by W.L.P., L.P.G., J.S.Y., and M.V.S.R. W.L.P., L.P.G., and M.V.S.R. wrote an initial manuscript draft that was critically edited by J.S.Y., W.L.P., M.E.P., and M.V.S.R., and approved by all authors.

## DECLARATION OF INTERESTS

The authors declare no competing interests.

## INCLUSION AND DIVERSITY

We support inclusive, diverse and equitable conduct of research.

## REFERENCES

1. Zeng, J.H., Liu, Y.X., Yuan, J., Wang, F.X., Wu, W.B., Li, J.X., Wang, L.F., Gao, H., Wang, Y., Dong, C.F., et al. (2020). First case of COVID-19 complicated with fulminant myocarditis: a case report and insights. Infection 48, 773–777. https://doi.org/10.1007/s15010-020-01424-5.

2. Li, Y., Li, H., Li, M., Zhang, L., and Xie, M. (2020). The prevalence, risk factors and outcome of cardiac dysfunction in hospitalized patients with COVID-19. Intensive Care Med. 46, 2096–2098. https://doi.org/10.1007/s00134-020-06205-0.

3. Lindner, D., Fitzek, A., Bräuninger, H., Aleshcheva, G., Edler, C., Meissner, K., Scherschel, K., Kirchhof, P., Escher, F., Schultheiss, H.P., et al. (2020). Association of cardiac infection with SARS-CoV-2 in confirmed COVID-19 autopsy cases. JAMA Cardiol. 5, 1281–1285. https://doi.org/10.1001/jamacardio.2020.3551.

4. Long, B., Brady, W.J., Koyfman, A., and Gottlieb, M. (2020). Cardiovascular complications in COVID-19. Am. J. Emerg. Med. 38, 1504–1507. https://doi.org/10.1016/j.ajem.2020.04.048.

5. Nishiga, M., Wang, D.W., Han, Y., Lewis, D.B., and Wu, J.C. (2020). COVID-19 and cardiovascular disease: from basic mechanisms to clinical perspectives. Nat. Rev. Cardiol. 17, 543–558. https://doi.org/10.1038/s41569-020-0413-9.

6. Langford, B.J., So, M., Raybardhan, S., Leung, V., Westwood, D., MacFadden, D.R., Soucy, J.P.R., and Daneman, N. (2020). Bacterial co-infection and secondary infection in patients with COVID-19: a living rapid review and meta-analysis. Clin. Microbiol. Infect. 26, 1622–1629. https://doi.org/10.1016/j.cmi.2020.07.016.

7. Kim, D., Quinn, J., Pinsky, B., Shah, N.H., and Brown, I. (2020). Rates of Co-infection between SARS-CoV-2 and other respiratory pathogens. JAMA 323, 2085–2086. https://doi.org/10.1001/jama.2020.6266.

8. Cheng, Y., Ma, J., Wang, H., Wang, X., Hu, Z., Li, H., Zhang, H., and Liu, X. (2021). Co-infection of influenza A virus and SARS-CoV-2: a retrospective cohort study. J. Med. Virol. 93, 2947–2954. https://doi.org/10.1002/jmv.26817.

9. Cuadrado-Payán, E., Montagud-Marrahi, E., Torres-Elorza, M., Bodro, M., Blasco, M., Poch, E., Soriano, A., and Piñeiro, G.J. (2020). SARS-CoV-2 and influenza virus co-infection. Lancet 395, e84. https://doi.org/10.1016/s0140-6736(20)31052-7.

10. Bao, L., Deng, W., Qi, F., Lv, Q., Song, Z., Liu, J., Gao, H., Wei, Q., Yu, P., Xu, Y., et al. (2021). Sequential infection with H1N1 and SARS-CoV-2 aggravated COVID-19 pathogenesis in a mammalian model, and co-vaccination as an effective method of prevention of COVID-19 and influenza. Signal Transduct. Targeted Ther. 6, 200. https://doi.org/10.1038/s41392-021-00618-z.

11. Bai, L., Zhao, Y., Dong, J., Liang, S., Guo, M., Liu, X., Wang, X., Huang, Z., Sun, X., Zhang, Z., et al. (2021). Coinfection with influenza A virus enhances SARS-CoV-2 infectivity. Cell Res. 31, 395–403. https://doi.org/10.1038/s41422-021-00473-1.

12. Chen, L., Li, X., Chen, M., Feng, Y., and Xiong, C. (2020). The ACE2 expression in human heart indicates new potential mechanism of heart injury among patients infected with SARS-CoV-2. Cardiovasc. Res. 116, 1097–1100. https://doi.org/10.1093/cvr/cvaa078.

13. Nicin, L., Abplanalp, W.T., Mellentin, H., Kattih, B., Tombor, L., John, D., Schmitto, J.D., Heineke, J., Emrich, F., Arsalan, M., et al. (2020). Cell type-specific expression of the putative SARS-CoV-2 receptor ACE2 in human hearts. Eur. Heart J. 41, 1804–1806. https://doi.org/10.1093/eurheartj/ehaa311.

14. Litviňuková, M., Talavera-López, C., Maatz, H., Reichart, D., Worth, C.L., Lindberg, E.L., Kanda, M., Polanski, K., Heinig, M., Lee, M., et al. (2020). Cells of the adult human heart. Nature 588, 466–472. https://doi.org/10.1038/s41586-020-2797-4.

15. Kenney, A.D., McMichael, T.M., Imas, A., Chesarino, N.M., Zhang, L., Dorn, L.E., Wu, Q., Alfaour, O., Amari, F., Chen, M., et al. (2019). IFITM3 protects the heart during influenza virus infection. Proc. Natl. Acad. Sci. USA 116, 18607–18612. https://doi.org/10.1073/pnas.1900784116.

16. Guy, J.L., Lambert, D.W., Warner, F.J., Hooper, N.M., and Turner, A.J. (2005). Membrane-associated zinc peptidase families: comparing ACE and ACE2. Biochim. Biophys. Acta 1751, 2–8. https://doi.org/10.1016/j.bbapap.2004.10.010.

17. Verdonk, K., Danser, A.H.J., and van Esch, J.H.M. (2012). Angiotensin II type 2 receptor agonists: where should they be applied? Expet Opin. Invest. Drugs 21, 501–513. https://doi.org/10.1517/13543784.2012.664131.

18. AbdAlla, S., Lother, H., Abdel-tawab, A.M., and Quitterer, U. (2001). The angiotensin II AT2 receptor is an AT1 receptor antagonist. J. Biol. Chem. 276, 39721–39726. https://doi.org/10.1074/jbc.M105253200.

19. Shajahan, A., Archer-Hartmann, S., Supekar, N.T., Gleinich, A.S., Heiss, C., and Azadi, P. (2021). Comprehensive characterization of N- and O- glycosylation of SARS-CoV-2 human receptor angiotensin converting enzyme 2. Glycobiology 31, 410–424. https://doi.org/10.1093/glycob/cwaa101.

20. Mehdipour, A.R., and Hummer, G. (2021). Dual nature of human ACE2 glycosylation in binding to SARS-CoV-2 spike. Proc. Natl. Acad. Sci. USA 118. e2100425118. https://doi.org/10.1073/pnas.2100425118.

21. Bartolomé, A., Liang, J., Wang, P., Ho, D.D., and Pajvani, U.B. (2020). Angiotensin converting enzyme 2 is a novel target of the γ-secretase complex. Preprint at bioRxiv. https://doi.org/10.1101/2020.09.01.277954.

22. Onabajo, O.O., Banday, A.R., Stanifer, M.L., Yan, W., Obajemu, A., Santer, D.M., Florez-Vargas, O., Piontkivska, H., Vargas, J.M., Ring, T.J., et al. (2020). Interferons and viruses induce a novel truncated ACE2 isoform and

not the full-length SARS-CoV-2 receptor. Nat. Genet. 52, 1283–1293. https://doi.org/10.1038/s41588-020-00731-9.

23. Ng, K.W., Attig, J., Bolland, W., Young, G.R., Major, J., Wrobel, A.G., Gamblin, S., Wack, A., and Kassiotis, G. (2020). Tissue-specific and interferon-inducible expression of nonfunctional ACE2 through endogenous retroelement co-option. Nat. Genet. 52, 1294–1302. https://doi.org/10.1038/s41588-020-00732-8.

24. Blume, C., Jackson, C.L., Spalluto, C.M., Legebeke, J., Nazlamova, L., Conforti, F., Perotin, J.M., Frank, M., Butler, J., Crispin, M., et al. (2021). A novel ACE2 isoform is expressed in human respiratory epithelia and is upregulated in response to interferons and RNA respiratory virus infection. Nat. Genet. 53, 205–214. https://doi.org/10.1038/s41588-020-00759-x.

25. Gordon, K., Redelinghuys, P., Schwager, S.L.U., Ehlers, M.R.W., Papageorgiou, A.C., Natesh, R., Acharya, K.R., and Sturrock, E.D. (2003). Deglycosylation, processing and crystallization of human testis angiotensin-converting enzyme. Biochem. J. 371, 437–442. https://doi.org/10.1042/bj20021842.

26. Schneider, C.A., Rasband, W.S., and Eliceiri, K.W. (2012). NIH Image to ImageJ: 25 years of image analysis. Nat. Methods 9, 671–675. https://doi.org/10.1038/nmeth.2089.

27. Yang, L., Han, Y., Nilsson-Payant, B.E., Gupta, V., Wang, P., Duan, X., Tang, X., Zhu, J., Zhao, Z., Jaffré, F., et al. (2020). A human pluripotent stem cell-based platform to study SARS-CoV-2 tropism and model virus infection in human cells and organoids. Cell Stem Cell 27, 125–136.e7. https://doi.org/10.1016/j.stem.2020.06.015.

28. Bojkova, D., Wagner, J.U.G., Shumliakivska, M., Aslan, G.S., Saleem, U., Hansen, A., Luxán, G., Günther, S., Pham, M.D., Krishnan, J., et al. (2020). SARS-CoV-2 infects and induces cytotoxic effects in human cardiomyocytes. Cardiovasc. Res. 116, 2207–2215. https://doi.org/10.1093/cvr/cvaa267.

29. Hayes, H.B., Nicolini, A.M., Arrowood, C.A., Chvatal, S.A., Wolfson, D.W., Cho, H.C., Sullivan, D.D., Chal, J., Fermini, B., Clements, M., et al. (2019). Novel method for action potential measurements from intact cardiac monolayers with multiwell microelectrode array technology. Sci. Rep. 9, 11893. https://doi.org/10.1038/s41598-019-48174-5.

30. Pradhapan, P., Kuusela, J., Viik, J., Aalto-Setälä, K., and Hyttinen, J. (2013). Cardiomyocyte MEA data analysis (CardioMDA)–a novel field potential data analysis software for pluripotent stem cell derived cardiomyocytes. PLoS One 8, e73637. https://doi.org/10.1371/journal.pone.0073637.

31. Marchiano, S., Hsiang, T.Y., Khanna, A., Higashi, T., Whitmore, L.S., Bargehr, J., Davaapil, H., Chang, J., Smith, E., Ong, L.P., et al. (2021). SARS-CoV-2 infects human pluripotent stem cell-derived cardiomyocytes, impairing electrical and mechanical function. Stem Cell Rep. 16, 478–492. https://doi.org/10.1016/j.stemcr.2021.02.008.

32. Zhu, H., Zhang, L., Ma, Y., Zhai, M., Xia, L., Liu, J., Yu, S., and Duan, W. (2021). The role of SARS-CoV-2 target ACE2 in cardiovascular diseases. J. Cell Mol. Med. 25, 1342–1349. https://doi.org/10.1111/jcmm.16239.

33. Dias-Peixoto, M.F., Santos, R.A.S., Gomes, E.R.M., Alves, M.N.M., Almeida, P.W.M., Greco, L., Rosa, M., Fauler, B., Bader, M., Alenina, N., and Guatimosim, S. (2008). Molecular mechanisms involved in the angiotensin-(1-7)/Mas signaling pathway in cardiomyocytes. Hypertension 52, 542–548. https://doi.org/10.1161/hypertensionaha.108.114280.

34. Akaberi, D., Krambrich, J., Ling, J., Luni, C., Hedenstierna, G., Järhult, J.D., Lennerstrand, J., and Lundkvist, Å. (2020). Mitigation of the replication of SARS-CoV-2 by nitric oxide in vitro. Redox Biol. 37, 101734. https://doi.org/10.1016/j.redox.2020.101734.

35. Heurich, A., Hofmann-Winkler, H., Gierer, S., Liepold, T., Jahn, O., and Pöhlmann, S. (2014). TMPRSS2 and ADAM17 cleave ACE2 differentially and only proteolysis by TMPRSS2 augments entry driven by the severe acute respiratory syndrome coronavirus spike protein. J. Virol. 88, 1293–1307. https://doi.org/10.1128/jvi.02202-13.

36. Nersisyan, S., Shkurnikov, M., Turchinovich, A., Knyazev, E., and Tonevitsky, A. (2020). Integrative analysis of miRNA and mRNA sequencing data reveals potential regulatory mechanisms of ACE2 and TMPRSS2. PLoS One 15, e0235987. https://doi.org/10.1371/journal.pone.0235987.

37. Pedersen, K.B., Chhabra, K.H., Nguyen, V.K., Xia, H., and Lazartigues, E. (2013). The transcription factor HNF1α induces expression of angiotensin-converting enzyme 2 (ACE2) in pancreatic islets from evolutionarily conserved promoter motifs. Biochim. Biophys. Acta 1829, 1225–1235. https://doi.org/10.1016/j.bbagrm.2013.09.007.

38. Davis, C.A., Hitz, B.C., Sloan, C.A., Chan, E.T., Davidson, J.M., Gabdank, I., Hilton, J.A., Jain, K., Baymuradov, U.K., Narayanan, A.K., et al. (2018). The Encyclopedia of DNA elements (ENCODE): data portal update. Nucleic Acids Res. 46, D794–D801. https://doi.org/10.1093/nar/gkx1081.

39. Kuan, T.C., Yang, T.H., Wen, C.H., Chen, M.Y., Lee, I.L., and Lin, C.S. (2011). Identifying the regulatory element for human angiotensin-converting enzyme 2 (ACE2) expression in human cardiofibroblasts. Peptides 32, 1832–1839. https://doi.org/10.1016/j.peptides.2011.08.009.

40. Ziegler, C.G.K., Allon, S.J., Nyquist, S.K., Mbano, I.M., Miao, V.N., Tzouanas, C.N., Cao, Y., Yousif, A.S., Bals, J., Hauser, B.M., et al. (2020). SARS-CoV-2 receptor ACE2 is an interferon-stimulated gene in human airway epithelial cells and is detected in specific cell subsets across tissues. Cell 181, 1016–1035.e19. https://doi.org/10.1016/j.cell.2020.04.035.

41. Sang, E.R., Tian, Y., Miller, L.C., and Sang, Y. (2021). Epigenetic evolution of ACE2 and IL-6 genes: non-canonical interferon-stimulated genes correlate to COVID-19 susceptibility in vertebrates. Genes 12, 154. https://doi.org/10.3390/genes12020154.

42. Chen, X., Liu, S., Goraya, M.U., Maarouf, M., Huang, S., and Chen, J.L. (2018). Host immune response to influenza A virus infection. Front. Immunol. 9, 320. https://doi.org/10.3389/fimmu.2018.00320.

43. Warner, F.J., Smith, A.I., Hooper, N.M., and Turner, A.J. (2004). Angiotensin-converting enzyme-2: a molecular and cellular perspective. Cell. Mol. Life Sci. 61, 2704–2713. https://doi.org/10.1007/s00018-004-4240-7.

44. Sharma, A., Garcia, G., Jr., Wang, Y., Plummer, J.T., Morizono, K., Arumugaswami, V., and Svendsen, C.N. (2020). Human iPSC-derived cardiomyocytes are susceptible to SARS-CoV-2 infection. Cell Rep. Med. 1, 100052. https://doi.org/10.1016/j.xcrm.2020.100052.

45. Sampaio, W.O., Souza dos Santos, R.A., Faria-Silva, R., da Mata Machado, L.T., Schiffrin, E.L., and Touyz, R.M. (2007). Angiotensin-(1-7) through receptor Mas mediates endothelial nitric oxide synthase activation via Akt-dependent pathways. Hypertension 49, 185–192. https://doi.org/10.1161/01.HYP.0000251865.35728.2f.

46. Bastard, P., Zhang, Q., Zhang, S.Y., Jouanguy, E., and Casanova, J.L. (2022). Type I interferons and SARS-CoV-2: from cells to organisms. Curr. Opin. Immunol. 74, 172–182. https://doi.org/10.1016/j.coi.2022.01.003.

47. Rimmelzwaan, G.F., Baars, M.M., de Lijster, P., Fouchier, R.A., and Osterhaus, A.D. (1999). Inhibition of influenza virus replication by nitric oxide. J. Virol. 73, 8880–8883. https://doi.org/10.1128/jvi.73.10.8880-8883.1999.

48. Klingström, J., Akerström, S., Hardestam, J., Stoltz, M., Simon, M., Falk, K.I., Mirazimi, A., Rottenberg, M., and Lundkvist, A. (2006). Nitric oxide and peroxynitrite have different antiviral effects against hantavirus replication and free mature virions. Eur. J. Immunol. 36, 2649–2657. https://doi.org/10.1002/eji.200535587.

49. Saura, M., Zaragoza, C., McMillan, A., Quick, R.A., Hohenadl, C., Lowenstein, J.M., and Lowenstein, C.J. (1999). An antiviral mechanism of nitric oxide: inhibition of a viral protease. Immunity 10, 21–28. https://doi.org/10.1016/s1074-7613(00)80003-5.

50. Croen, K.D. (1993). Evidence for antiviral effect of nitric oxide. Inhibition of herpes simplex virus type 1 replication. J. Clin. Invest. 91, 2446–2452. https://doi.org/10.1172/jci116479.

51. Tavazzi, G., Pellegrini, C., Maurelli, M., Belliato, M., Sciutti, F., Bottazzi, A., Sepe, P.A., Resasco, T., Camporotondo, R., Bruno, R., et al. (2020). Myocardial localization of coronavirus in COVID-19 cardiogenic shock. Eur. J. Heart Fail. 22, 911–915. https://doi.org/10.1002/ejhf.1828.

52. Puelles, V.G., Lütgehetmann, M., Lindenmeyer, M.T., Sperhake, J.P., Wong, M.N., Allweiss, L., Chilla, S., Heinemann, A., Wanner, N., Liu, S., et al. (2020). Multiorgan and renal tropism of SARS-CoV-2. N. Engl. J. Med. *383*, 590–592. https://doi.org/10.1056/NEJMc2011400.

53. Rajaram, M.V.S., Arnett, E., Azad, A.K., Guirado, E., Ni, B., Gerberick, A.D., He, L.Z., Keler, T., Thomas, L.J., Lafuse, W.P., and Schlesinger, L.S. (2017). M. tuberculosis-initiated human mannose receptor signaling regulates macrophage recognition and vesicle trafficking by FcRgamma-chain, Grb2, and SHP-1. Cell Rep. *21*, 126–140. https://doi.org/10.1016/j.celrep.2017.09.034.

54. Wu, Q., Hossfeld, A., Gerberick, A., Saljoughian, N., Tiwari, C., Mehra, S., Ganesan, L.P., Wozniak, D.J., and Rajaram, M.V.S. (2019). Effect of Mycobacterium tuberculosis enhancement of macrophage P-glycoprotein expression and activity on intracellular survival during antituberculosis drug treatment. J. Infect. Dis. *220*, 1989–1998. https://doi.org/10.1093/infdis/jiz405.

55. Moltedo, B., Li, W., Yount, J.S., and Moran, T.M. (2011). Unique type I interferon responses determine the functional fate of migratory lung dendritic cells during influenza virus infection. PLoS Pathog. *7*, e1002345. https://doi.org/10.1371/journal.ppat.1002345.

56. Makvandi-Nejad, S., Laurenson-Schafer, H., Wang, L., Wellington, D., Zhao, Y., Jin, B., Qin, L., Kite, K., Moghadam, H.K., Song, C., et al. (2018). Lack of truncated IFITM3 transcripts in cells homozygous for the rs12252-C variant that is associated with severe influenza infection. J. Infect. Dis. *217*, 257–262. https://doi.org/10.1093/infdis/jix512.

57. Shi, G., Kenney, A.D., Kudryashova, E., Zani, A., Zhang, L., Lai, K.K., Hall-Stoodley, L., Robinson, R.T., Kudryashov, D.S., Compton, A.A., and Yount, J.S. (2021). Opposing activities of IFITM proteins in SARS-CoV-2 infection. EMBO J. *40*, e106501. https://doi.org/10.15252/embj.2020106501.

58. Leist, S.R., Dinnon, K.H., 3rd, Schäfer, A., Tse, L.V., Okuda, K., Hou, Y.J., West, A., Edwards, C.E., Sanders, W., Fritch, E.J., et al. (2020). A mouse-adapted SARS-CoV-2 induces acute lung injury and mortality in standard laboratory mice. Cell *183*, 1070–1085.e12. https://doi.org/10.1016/j.cell.2020.09.050.

# STAR★METHODS

## KEY RESOURCES TABLE

| REAGENT or RESOURCE | SOURCE | IDENTIFIER |
|---|---|---|
| **Antibodies** | | |
| Rabbit Anti-ACE2 antibody | Sino Biologicals | Cat# 10108-T56 and T60 |
| Goat anti mouse ACE2 antibody | Invitrogen | Cat# PA5-47488; RRID AB_2606505 |
| CD326/EpCam mouse mAb G8.8 clone | eBiosciences | Cat# 4-5791-81; RRID AB-953624 |
| Rat mAb F4/80 | AbD Serotech | Cat # MCA497G; RRID AB_872005 |
| Isotype control rabbit IgG | Abcam | Cat # ab172730; RRID AB_2687931 |
| Isotype control rat IgG | BioRad | Cat # 305005; RRID AB_619912 |
| Rabbit anti mouse IgG (Alexa Fluor-488) conjugated secondary Ab | Thermo Fisher Scientific | Cat# A27023; RRID AB_2536087 |
| anti-β actin antibody | Santa Cruz Biotechnology | Cat# SC-1616; RRID AB_630836 |
| anti-alveolar type II epithelial cell markers SP-C Rabbit monoclonal antibody (mAb) | Abcam | Cat# Ab211326 |
| Goat antiRabbit IgG (Alexa Fluor-594) conjugated secondary Ab (ab150080; Abcam) | Abcam | Cat# ab150080; RRID AB_2650602 |
| SARS-CoV-2, 2019-nCoV spike protein-RBD | Sino Biologicals | Cat # 40592-V08H-B |
| **Bacterial and virus strains** | | |
| Influenza virus A/PR/8/1934 (H1N1) (PR8) | Dr. Thomas Moran and Dr. Bruno Moltedo (Icahn School of Medicine at Mt. Sinai, New York) | Moltedo et al.,[55] |
| Influenza virus strain A/Puerto Rico/8/1934 (H1N1) ΔNS1 | Dr. Thomas Moran and Dr. Bruno Moltedo (Icahn School of Medicine at Mt. Sinai, New York) | Moltedo et al.,[55] |
| Influenza virus strain A/California/04/2009 (H1N1) | BEI Resources | Cat# NR-13658 |
| Influenza virus strain A/Victoria/361/2011(H3N2) | BEI Resources | Cat# NR-44024 |
| Influenza virus strain B/Texas/06/2011 (Yamagata) | BEI Resources | Cat# NR-44024 |
| Sendai virus (SeV) strain Cantell | ATCC | Cat# VR-907 |
| Human metapneumovirus (MPV), strain NL/1/00 (A1) | Generated by Dr. Jianrong Li (Ohio State University) | Dr. Li, Ohio State University[56] |
| SARS-CoV-2 USA-WA1/2020 stock was obtained from BEI Resources (Cat #R52281) | BEI Resources | Cat #R52281) |
| The mouse-adapted SARS-CoV-2 variant strain MA10, | Generated by the laboratory of Dr. Ralph Baric Leist et al.[57] | BEI resources (Cat# NR-55329) |
| **Biological samples** | | |
| Embryonated chicken eggs | Charles River Laboratories | |
| Human Lung sections | Department of Pathology, College of Medicine | The Ohio State University |
| **Chemicals, peptides and recombinant proteins** | | |
| Human cardiac fibroblast growth medium | Promo Cell (Heidelberg, Germany) | Cat# C-23025 |
| hiPSC-CMs plating medium | Fujifilm Cellular Dynamic Inc. (CDI, Madison, WI, USA) | Cat# M1001 |
| hiPSC-CMs maintenance medium | Fujifilm Cellular Dynamic Inc. (CDI, Madison, WI, USA) | Cat# M1003 |

*Continued*

| REAGENT or RESOURCE | SOURCE | IDENTIFIER |
|---|---|---|
| Fibronectin | Millipore Sigma CA, USA | Cat #F0895 |
| 0.1% Gelatin solution | Stem Cell Technologies Inc., USA | Cat # 07903 |
| 4% paraformaldehyde | Thermo Fisher Scientific | Cat# J19943-K2 |
| S-Nitroso-N-acetylpenicillamine | Sigma (St. Louis, MO, USA) | Cat# 487910 |
| N-Acetyl-D-penicillamine | Sigma (St. Louis, MO, USA) | Cat# 01423 |
| MEA 24-well CytoView MEA culture plate | Axion Bio Systems, GA, USA | Cat# M384-tMEA-24W |
| DNA stain 4′.6-diamidino-2-phenylindole, dihydrochloride (DAPI) | Molecular Probes | Cat# D1306 |
| SYBR Green Supermix | Bio-Rad | Cat# 1725124 |
| Qiagen buffer RLT | QIAGEN | Cat # 79216 |
| **Critical commercial assays** | | |
| Mycoplasma detection kit | AmericanType Culture Collection | Cat# R30-1012K TM |
| Cytotoxicity Detection Kit | Millipore Sigma, USA | Cat # 11 644 793 001 |
| RNeasy Mini Kit | Qiagen, | Cat # 74104 |
| SARS-CoV-2 RT-qPCR detection kit | ScienCell Research Laboratories | Cat # RU7038 |
| Rapid Molecular Influenza A/B Testing | Abbott | Cat # 427000 |
| BCA Protein Assay Kit | Pierce | Cat# 23225 |
| Glycoprotein Deglycosylation Kit | Sigma | Cat # 362280 |
| Greiss Reagent System | Promega | Cat# TB229 |
| ACE2 activity kit | Bio vision | Cat# K897 |
| **Experimental models: Cell lines** | | |
| Human lung epithelial cells (A549) | AmericanType Culture Collection | Cat# CRM-CCL-185 |
| Vero E6 | AmericanType Culture Collection | Cat# CRL-1586 |
| Human lung fibroblasts | AmericanType Culture Collection | Cat# CCL-186 |
| Primary Human cardiac fibroblasts | Promo Cell, Heidelberg, Germany | Cat# C-12375 |
| Human induced pluripotent stem cell-derived cardiomyocytes | Fujifilm Cellular Dynamics Inc. Madison, WI, USA | Cat# C1006 |
| Human monocyte derived macrophages from PBMCs isolated from healthy donors | Rajaram et al.,[54] | Rajaram lab |
| Human bronchial epithelial cells | Cure Cystic Fibrosis Columbus (C3) Epithelial Cell Core (ECC) | Nationwide Children's Hospital and The Ohio State University |
| **Experimental models: Organisms/strains** | | |
| C57BL/6 male mice 12 weeks of age | The Jackson Laboratory | Cat# 000664 |
| **Software and algorithms** | | |
| Axis Navigator and cardiac analysis tool (CAT) | Axion BioSystem (Atlanta, GA, USA) | www.axionbiosystems.com |
| GraphPad Prism 6 version | GraphPad | https://www.graphpad.com/ |
| FlowJo software | Tree Star | |
| ImageJ | National Institute of Health Schneider et al.,[26] | https://imagej.nih.gov/ij/ |
| **Other** | | |
| BD LSR Fortessa™ cell analyzer (BD Biosciences) and output analyzed using FlowJo software (Tree Star). | BD biosciences | https://www.bdbiosciences.com |
| Molecular Devices Plate Reader | Molecular Devices | www.moleculardevices.com |
| CFX96 (Bio-Rad) machine | Bio-Rad | https://www.bio-rad.com |
| Flow View 1000 Laser Scanning Confocal microscope | (Olympus) | https://www.olympus-lifescience.com |

## RESOURCE AVAILABILITY

### Lead contact

Requests for resources and reagents should be directed to the lead contact M.V.S.R (rajaram.3@osu.edu).

### Materials availability

All reagents and materials will be made available on request after completion of Materials Transfer Agreement.

### Data and code availability

- All data reported in this paper will be shared by the lead contact upon request.

- This paper does not report original code.

- Any additional information required to reanalyze the data in this paper is available upon request from the lead contact.

## EXPERIMENTAL MODEL AND SUBJECT DETAILS

### Cell lines

Human lung epithelial cells (A549) (ATCC CRM-CCl-185), Vero E6 (CRL1586), human lung fibroblasts (CCL-186) were obtained from AmericanType Culture Collection (Manassas, VA, USA). Primary Human cardiac fibroblasts (C-12375) and Human induced pluripotent stem cell-derived cardiomyocytes (hiPSC-CMs), were from PromoCell (Heidelberg, Germany) and Fujifilm Cellular Dynamics Inc. (Cat# C1006, CDI, Madison, WI, USA), respectively. Human monocyte derived macrophages were differentiated from PBMCs isolated from healthy donors.[53] All cell lines were routinely tested for Mycoplasma contaminations with the Universal Mycoplasma Detection Kit (ATCC R 30–1012K TM).

### Human lung section

Lung sections from diseased IAV and IBV infected and non-lung related disease were obtained from Department of Pathology, College of Medicine, and The Ohio State University.

### Mouse strains

C57Bl/6 mice used in this study have been purchased from Jackson Laboratory, and maintained in University laboratory Animal Resources facility at The Ohio State University. We used 12 weeksold male mice for this study. Mice were maintained on a 12:12h light cycle at 30–70% humidity with standard water and chow. All animal handling and infections were performed according to OSU laboratory animal care and use program guidelines.

## METHOD DETAILS

### Cell culture media and reagents

Dulbecco's PBS with and without $Ca^{2+}$ and $Mg^{2+}$, RPMI 1640 medium with L-glutamine (RPMI), F-12K medium and HEPES buffer were from GIBCO-Invitrogen (Invitrogen Life Technologies, Carlsbad, CA, USA). Heat-inactivated Hyclone Standard FBS were from Thermo Fisher Scientific Inc. (Waltham, MA, USA). Human cardiac fibroblast growth medium (C-23025) was purchased from Promo Cell (Heidelberg, Germany). The hiPSC-CMs plating medium (Cat# M1001) and maintenance medium (Cat# M1003) were purchased from Fujifilm Cellular Dynamics Inc. (CDI, Madison, WI, USA). Fibronectin was obtained from Millipore Sigma CA, USA (Cat#F0895), and 0.1% Gelatin solution was procured from STEMCELL Technologies Inc.,USA (Cat# 07903). Anti-ACE2 antibody (10108-T56 and T60) and anti-SARS-CoV-2 Nucleocapsid antibody (40143-MM08) was from Sino Biological. Anti-TMPRSS2 antibody (MA5-35756), Streptavidin 488 (Cat#S11223), anti-mouse secondary antibody conjugated with Alexa Fluor 488, and 4% paraformaldehyde were obtained from Thermo Fisher Scientific. Anti- β-actin antibody (SC-1616) was obtained from Santa Cruz Biotechnology. The (±)-S-Nitroso-N-acetylpenicillamine (487910) and N-Acetyl-D-penicillamine were purchased from Sigma (St. Louis, MO, USA).

### Culture of human induced pluripotent stem cell-derived cardiomyocytes

Human iPSC-CMs were plated using the supplier protocol. Briefly, hiPSC-CMs were plated as a monolayer in sterile 12 well cell culture plates coated with 0.1% gelatin and incubated at 37°C and 5% $CO_2$ in a

humidified atmosphere for 48h. Then cells were transferred into CDI maintenance medium for further culture and the maintenance medium was changed every alternate day. For, gelatin coating, 1mL of 0.1% gelatin was added into each well of a 12 well plate and incubated at 37°C for a minimum of 1h.

### Human iPSC-CMs functional analysis with the multi-electrode array (MEA) system

After 5–7 days of culturing hiPSC-CMs in 12-well cell culture plates, the cells were replanted onto an MEA 24-well CytoView MEA culture plate (Cat#M384-tMEA-24W, Axion BioSystem, GA, USA) coated with fibronectin (50 μg/mL). For MEA plate coating, 5 μL fibronectin was added as a single drop into the center of each MEA well and incubated at, 37°C, 5% $CO_2$ in a humidified air for a minimum of 1h. The hiPSC-CMs were harvested using 0.25% Trypsin-EDTA, washed by centrifugation and 5 μL hiPSC-CMs ($0.03 \times 10^6$ cells/well) were seeded into the center of the MEA plate. Plates were incubated for 1–2 hat 37°C, 5% $CO_2$ in a humidified air. Finally, 500 μL CDI maintenance medium was added into each well and cultured at 37°C and 5% $CO_2$ in a humidified atmosphere and the maintenance medium was changed every alternate day. Human iPSC-CMs were incubated with heat killed SARS-CoV-2 at an MOI of 1 and 2.5, spike protein, spike RBD or left untreated, and the electrical signal was recorded using the MEA system every 15 min for 6 h. The data was processed using Axis Navigator and cardiac analysis tool (CAT), Axion Bio System (Atlanta, GA, USA).

### Isolation and culture of human monocyte-derived macrophages (MDMs)

MDM monolayers were prepared from healthy human volunteers using an approved OSU IRB protocol, as described.[54] Briefly, PBMCs were isolated from heparinized blood on a Ficoll cushion and then cultured in Teflon wells (Savillex, Minnetonka, MN, USA) for 5 days in the presence of 20% autologous serum. The wells were then placed on ice for 30 min and the unattached PBMCs were removed by washing. MDMs in the cultured PBMCs were adhered to 12-well or 24-well tissue culture plates (Falcon, Becton Dickinson lab ware, Franklin Lakes, NJ, USA) for 2-3h in 10% autologous serum. Lymphocytes were removed by washing, replaced with RPMI containing 10% autologous serum and incubated overnight.

### Viral strains

Influenza virus strain A/Puerto Rico/8/1934 (H1N1) pdm09 and Influenza virus strain A/Puerto Rico/8/1934 (H1N1) ΔNS1, provided by Dr. Thomas Moran and Dr. Bruno Moltedo (Icahn School of Medicine at Mt. Sinai, New York),[55] and propagated in specific pathogen free 10-day and 6-day embryonated chicken eggs. Influenza virus strain A/California/04/2009 (H1N1), NR-13658 was purchased from BEI Resources and propagated in MDCK cells. Influenza virus strain A/Victoria/361/2011 (H3N2) and Influenza virus strain B/Texas/06/2011 (Yamagata), NR-44024 were purchased from BEI Resources propagated in specific pathogen free 10-day embryonated chicken eggs. Sendai virus (SeV) strain Cantell, VR-907 was purchased from ATCC, propagated in specific pathogen free 10-day embryonated chicken eggs. Human metapneumovirus (MPV), strain NL/1/00 (A1), generated by reverse genetics in the laboratory of Dr. Jianrong Li (Ohio State University) as previously described[56] and propagated on Vero E6 cells.

### Influenza A virus propagation and tittering

Influenza virus A/PR/8/1934 (H1N1) (PR8) were provided by Dr. Thomas Moran and Dr. Bruno Moltedo (Icahn School of Medicine at Mt. Sinai, New York)[55] and were propagated in 10-day-old embryonated chicken eggs (Charles River Laboratories) for 48 hours at 37°C and tittered in MDCK cells.

### SARS-CoV-2 propagation and tittering

SARS-CoV-2 USA-WA1/2020 stock was obtained from BEI Resources (Cat #R52281), and propagated once in Vero E6 cells as described previously.[57] Briefly, the SARS-CoV-2 stock was diluted 1:10,000 in DMEM and added to confluent Vero E6 cells for 1 hat 37°C. Following the 1 h inoculation period, virus-containing media was replaced with DMEM containing 4% FBS and incubated at 37°C for 72 hat which point significant cytopathic effect was observed. Cell supernatant containing infectious virus was centrifuged at 1,000× g for 10 min to remove cell debris, and was aliquoted, flash frozen in liquid nitrogen, and stored at −80°C. Virus titer was determined by TCID50 assay in Vero cells using the presence of cytopathic effect coupled with viral N protein staining for identification of infected wells. The viral stock titer was further confirmed by standard plaque assay with 0.3% agarose (Sigma) overlay and visualization with 0.25% Crystal Violet (Sigma) in Vero cells. Full genome sequencing of the virus stock by the Ohio State University Medical Center Clinical Diagnostics Laboratory confirming the strain identity.[57] The mouse-adapted SARS-CoV-2

variant strain MA10, generated by the laboratory of Ralph Baric (University of North Carolina, Chapel Hill, NC),[58] were obtained from BEI Resources (Cat # NR-55329) and propagated once in Vero-E6 cells.

### Influenza A virus and SARS CoV-2 coinfections analyzed by flow cytometry

Cells were inoculated with IAV (MOI 1) in serum free media for 30 min, washed with warm RPMI and incubated in RPMI with 5% FBS at 37°C for an additional 48 h, and the cells were washed with warm RPMI and replenished with RPMI (no serum media) before being inoculated with SARS-CoV-2 (MOI 2)for 1hour and washed with warm media and replaced with RPMI with 5% FBS for 24 h or the indicated time points. The cells were washed and fixed with 4% paraformaldehyde (Thermo Scientific) for 1 hat room temperature, permeabilized with PBS containing 0.1% TritonX-100, and blocked with PBS containing 2% FBS. Cells were then stained with anti-SARS-CoV-2 Nucleocapsid antibody (Sino Biological, 40143-MM08) followed by anti-mouse secondary antibody conjugated with Alexa Fluor 488 (Life technologies). Stained cell suspensions were processed on a BD LSR Fortessa™ cell analyzer (BD Biosciences) and output analyzed using FlowJo software (Tree Star). Infected cell gates were set using uninfected control samples.

### Influenza A virus and SARS-CoV-2 coinfections examined by confocal microscopy

Influenza A virus or SARS-CoV-2-infected A-549, human cardiac fibroblasts and hiPSC-CMs were washed in PBS, fixed with 4% paraformaldehyde (Thermo Fisher Scientific) for 1 hat room temperature, then blocked in blocking reagent (5% BSA, 10% FBS in PBS). Coverslips were incubated with anti ACE2 Ab (10108-T60), antiSARS-CoV-2 nucleocapsid protein Ab (40143-MM08) from Sino Biologicals, anti-influenza A virus nucleoprotein mAb 2F4 (NR-19868) from BEI resources, or the appropriate isotype control (Rabbit IgG-ab172730; Mouse IgG1-ab81216; Rat IgG;305005) for 1 hat room temperature, washed with blocking reagent, and counterstained with Goat anti rabbit IgG (Alexa Fluor-594) conjugated secondary Ab (ab150077) and Goat anti-mouse IgG1 (Alexa Fluor-488) conjugated secondary Ab (A-21121) for 1 hat room temperature. Nuclei were labeled with the DNA stain 4'.6-diamidino-2-phenylindole, dihydrochloride (DAPI) (D1306; Molecular Probes). Finally, coverslips were washed and mounted on glass slides and viewed using an Olympus Flowview confocal microscope.

### Influenza A virus and SARS-CoV-2 coinfection viral titer assay

Viral titer assays were performed on cell culture supernatants from IAV and SARS-CoV-2 co-infected A549, HCF and hiPSC-CMs by TCID50 measurements using 10-fold serial dilutions assayed on triplicate wells of Vero E6 cells. The presence of virus replication in each well was assessed by visual examination of cytopathic effect along with antibody staining for SARS-CoV-2 N protein antigen (mouse mAb 40143-MM08, Sino Biological) followed by detection with fluorescent secondary antibody. TCID50 titers were calculated using the Reed-Muench method. Viral titers in lung and heart homogenates of IAV alone or IAV with SARS-CoV-2 co-infected mice were measured as described above.

### Cell cytotoxicity assay

Cell cytotoxicity was determined with a Cytotoxicity Detection Kit (Millipore Sigma, USA) measuring lactate dehydrogenase (LDH) activity released from damaged cells, according to the manufacturer's instructions. Cells were infected as previously described. At 24, 48 and 72 h after infection, 25μL of the medium over the duplicate cultures was transferred to a 96-well plate, mixed with 25 μL of the LDH cytotoxicity assay reagent, and incubated at 37°C for 30 min. Stop solution (25 μL) was added, and the optical density at 492 nm ($OD_{492nm}$) was directly measured using a Molecular Devices Plate Reader. The percent cytotoxicity was calculated according to the manufacturer's instructions.

### ACE2 and SARS-CoV-2 quantification by real time qRT-CPR

Expression of ACE2 and delta ACE2 in IAV infection were determined by qRT-PCR of duplicate samples using IQ SYBR Green Supermix (Bio-Rad). Briefly, A549 and HCF cells were inoculated with IAV (MOI of 2) and after 24 and 48 h post infection, total RNA was extracted. RNA was reverse-transcribed using random primers by the Promega Reverse Transcription System (Thermal Fisher Scientific). The amplification conditions were 95°C for 2 min, followed by 45 cycles of 95°C for 15s, 60°C for 30s, and 72°C for 30s. Previously described ACE2 primers (forward GGGCGACTTCAGGATCCTTAT; reverse GGATATGCCCCATCTCATGATG) and dACE2 (forward GGAAG CAGGCTGGGACAAA; reverse AGCTGTCAGGAAGTCGTCCATT) were used.[22] Expression of mRNA was calculated by the Δ threshold cycle method using β-actin as the normalizer. Levels of ACE2 and dACE2 in IAV-infected cells were expressed relative to uninfected cells. SARS-CoV-2-infected A549, HCF and hiPSC-CMs

were lysed with Qiagen buffer RLT (QIAGEN, 79216) supplemented with 1% β-mercaptoethanol (Bio-Rad, 1610710). RNA was isolated using the RNeasy Mini Kit (QIAGEN, 74104) and quantified using the NanoDrop 2000c (ThermoFisher). Viral load was measured by detection of the viral nucleocapsid gene by one-step quantitative real-time PCR using TaqProbe RT-qPCR master mix (SARS-CoV-2 RT-qPCR detection kit; RU7038; ScienCell Research laboratories) with two sets of primers (N1 and N2) and probes specific to the SARS-CoV-2 nucleocapsid gene with the human RPP30 as the internal reference. RT-qPCR reactions were performed on a CFX96 (Bio-Rad) machine with amplification conditions indicated by the manufacturer (ScienCell Research Laboratories). Expression was determined by the Δ threshold cycle method using Human RPP30 as the normalizer. Expression levels of the nucleocaspsid transcript were expressed relative to human RPP30 levels.

### Mouse infection and histology

C57BL/6 (8-10-week old) mice were anesthetized with isoflurane (Henry Schein Animal Health) and intranasally infected with IAV strain PR8 ($1 \times 10^4$ PFU) in sterile saline, or mock infected with saline in some experiments. Mice were monitored daily for weight loss and morbidity, and sacrificed if weight loss exceeded 30% of starting body mass. All procedures were approved by the OSU IACUC. IAV-infected mouse lungs and hearts were harvested after 6 days of infection or at days 0, 4, 8, 12 and 16, and the lung lobes/hearts were fixed with 10% neutral buffered formalin, embedded in paraffin, sectioned, and stained with antibodies to different antigens, as described previously.[54] Briefly, tissue sections were first deparaffinized with xylene, followed by rehydration with graded alcohols (100%, 95%). A heat-induced epitope retrieval procedure was carried out by heating the tissue slides in citrate buffer (pH 6.0) at 95°C for 10 min. Each tissue section was rehydrated with PBS buffer, blocked (5% nonfat dry milk in PBS +0.01% sodium azide) for 3 hat room temperature, and then incubated with specific primary Abs using manufacturer-recommended dilutions in a humidified chamber at 4°C overnight. The sections were incubated with antibodies to ACE2 (Goat anti mouse; PA5-47488 from Invitrogen), alveolar type II epithelial cell markers SP-C (Rabbit monoclonal; ab211326 from Abcam) and CD326/EpCam (Mouse monoclonal; G8.8; 14-5791-81 from eBiosciences) and a macrophage marker (Rat monoclonal F4/80; MCA497G; AbD Serotec) or the appropriate isotype control (Rabbit IgG; ab172730; Rat IgG; 305005 from Abcam) for 1 hat room temperature, washed with blocking reagent, and counterstained with Rabbit anti mouse IgG (Alexa Fluor-488) conjugated secondary Ab (A27023; ThermoFisher Scientific), Goat antiRabbit IgG (Alexa Fluor-594) conjugated secondary Ab (ab150080; Abcam) for 1 hat room temperature. Nuclei were labeled with the DNA stain 4'.6-diamidino-2-phenylindole, dihydrochloride (DAPI) (D1306; Molecular Probes). After washing and drying at room temperature, the slides were examined by a Flow View 1000 Laser Scanning Confocal microscope (Olympus). Heart tissues were homogenized in Trizol and followed by RNA extraction, as described above. qRT-PCR was performed as previously described.

### Demography of human lung samples and histology

Human tissue was collected at the time of autopsy within 48 hours of death from 5 female and 5 male patients ranging in age from 30 to 67 years old. Influenza A (1 male and 2 female) or B (1 male and 1 female) was detected 72 hours before death by ID NOW Rapid Molecular Influenza A/B Testing (Abbott). All influenza A/B positive patients developed bronchopneumonia. Representative sections of lungs were collected from patients with influenza A or B and normal controls. The lung sections were processed as described above and stained with human ACE2 antibody with rabbit anti-ACE2 antibody (10108-T56 and T60, Sino Biological) followed by Goat antiRabbit IgG (AF488) conjugated secondary antibody (ab150081 from Abcam) and nuclei were labeled with DAPI.

### *In vivo* influenza A virus and SARS-CoV-2 coinfection studies

C57BL/6 (8-10-week old) mice were anesthetized with isoflurane (Henry Schein Animal Health) and intranasally infected with IAV strain PR8 ($1 \times 10^4$ PFU) in sterile saline. After 5 days, the influenza A virus-infected mice and uninfected mice were intranasally infected with mouse adapted SARS-CoV-2 strain MA10 ($1 \times 10^5$ PFU). All mice were housed in a pathogen free animal facility, and experiments were conducted with approval of the Animal Care and Use Committee at The Ohio State University, which is accredited by the American Association of Accreditation of Laboratory Animal Care International according to guidelines of the Public Health Services as described in the guide for the Care and Use of Laboratory Animals.

## Cell/tissue lysis and immunoblotting

After infection/treatment, cell monolayers or tissue samples were washed once in PBS and lysed in TN-1 lysis buffer or tissue lysis buffer at 4°C for 10 min and centrifuged at 10,000 × *g* for 10 min at 4°C to remove cell debris.[53] Protein concentrations of the cleared lysates were measured by the BCA Protein Assay Kit (Pierce). Protein-matched total cell lysates were separated by SDS-PAGE and analyzed by IB using the following Abs: rabbit anti-ACE2 antibody (10108-T56 and T60) from Sino Biological, anti-TMPRSS2 antibody (MA5-35756) from ThermoFisher Scientific and β-actin antibody (SC-1616) from Santa Cruz Biotechnology.

## Protein de-glycosylation assay

A Glycoprotein Deglycosylation Kit (Sigma; #362280) was used according to manufacturer instructions. Briefly, cell lysates (200μg) from uninfected and IAV-infected A549, HCF, hiPSC-CMs and Vero E−6 cells were mixed with 10 μL of 5× reaction buffer and 2.5 μL denaturation solution and heated at 100°C for 5 min, cooled down and incubated with 2.5 μL of Triton X-100. The lysates were de-glycosylated by the addition of 1 μL each of N-Glycosidase F, α 2–3,6,8,9-neuraminidase, Endo-α-N-acetylgalactosaminidase, β1,4-galactosidase, and β-N-Acetylyglucosaminidase, and incubation at 37°C for 3 h. An aliquot was mixed with SDS-PAGE loading buffer and 10 μL were loaded on gels for immunoblot (IB) assays with anti-ACE2 antibody.

## Griess reagent $NO_2^-$ assay

Cell culture supernatants from A549, HCF and hiPSC-CMs cells infected with IAV and SARS-CoV2 or uninfected cells were harvested and used to determine NO production by measuring the amount of nitrite ($NO_2^-$) production using Greiss Reagent System TB229 (Promega) according to the manufacturer's instructions. Briefly, 50 μL of culture supernatants were mixed with 50 μL of Sulfanilamide solution and the samples incubated at room temperature for 10 min in the dark and then mixed with 50 μL of N-1napthyllethylenediamine dihydrochloride (NED). The mixture was incubated at room temperature for 10 min in the dark and absorbance was measured at 540 nm using a Molecular Devices plate reader. The $NO_2^-$ concentration was calculated from a nitrite standard curve.

## SARS-CoV-2 spike protein binding to ACE2

A549 and HCF cells were cultured on coverslips (2 × 10^{4} cells/well) and after overnight incubation, cells were infected with IAV (MOI 1 viral particle/cell). After 48 h, cells were treated with 2 ng/mL of recombinant biotinylated SARS-CoV-2 spike protein RBD (SARS-CoV-2, 2019-nCoV spike protein-RBD, Cat#40592-V08H-B, Sino Biological) for 1 hat 37°C. Cells were washed twice with warm media and stained with 5 μg/mL streptavidin 488 (Cat#S11223; Thermo Fisher Scientific) for 30 min at 37°C. Cells were washed twice with PBS and fixed with 4% paraformaldehyde (Thermo Fisher Scientific) for 30 min. The coverslips were washed with PBS and the nuclei were labeled with the DNA stain 4′.6-diamidino-2-phenylindole, dihydro-chloride (DAPI) (D1306; Molecular Probes). Finally, coverslips were washed and mounted on glass slides with Pro-Long™ Gold anti-fade reagent and viewed using an Olympus Flow view confocal microscope. To test whether IAV mediated induction of ACE2 in human lungs shows an increased binding of spike protein, lung sections from deceased IAV patients (n = 3), IBV patients (n = 2), and non-lung related disease patients were incubated with 2 ng/mL of recombinant biotinylated SARS-CoV-2 spike protein RBD for 1 hat 37°C, slides were washed, and stained with streptavidin 488 (5μg/mL) for 1 h. Slides were washed and the nuclei were stained with DAPI. The lung sections were examined by confocal microscopy. Human lung sections were obtained from Department of Pathology at The Ohio State University Wexner Medical Center, Columbus, OH, USA.

## ACE2 peptidase activity assays

A549, HCF, and hiPSC-CMs cells were either uninfected or infected with IAV or SARS-CoV-2 and after 48 h (IAV infection) and 24 h (SARS-CoV-2), the cells were lysed with 400 μL of Lysis Buffer in the ACE2 activity kit (#K897, Bio Vision). ACE2 peptidase activity was measured according to the manufacturer's instructions. Briefly, 5 μL of cell lysates were added to a 96-well plate in duplicate wells, along with background control (5 μL of lysis buffer), positive control (2 μL of diluted ACE2), and negative control (2 μL of diluted ACE2 in-hibitor) added to wells containing sample and/or ACE2 positive control. The volume was adjusted to 50 μL/well with ACE2 assay buffer. The assay reaction was initiated by adding 50 μL of substrate mix and the fluorescence (Ex/Em = 320/420 nm) was measured in a kinetic mode for 120 min at room temperature.

Protein concentrations of the lysates were measured by the BCA Protein Assay Kit (Pierce). The ACE2 activity was calculated based on the manufacturer's instructions.

### Total RNA sequencing and data analysis

Total RNA was extracted from influenza A virus (IAV) infected HCF and hiPSC-CMs at 48 h post infection with TRIzol (Thermo Fisher Scientific, Cat# 15596026) and RNAeasy kit (QIAGEN, Cat# ID74106), according to the manufacturer's instructions. RNA quantity and quality was measured and complimentary cDNA libraries were made and sequenced on an Illumina NovaSeq SP flow cell (pair-end, 150 bp format, 35 to 40 million clusters, equivalent to 70–80 million reads) by the Genomic Core at Nationwide Children's Hospital. The sequencing data processing and analysis were performed by the OSU Bioinformatics Shared Resources Group.

### Biosafety

All work with live SARS-CoV-2 was performed at Biosafety Level 3 (BSL3) according to standard operating procedures approved by the Ohio State University BSL3 Operations Group and Institutional Biosafety Committee. Samples were removed from the BSL3 facility for flow cytometry analysis and confocal microscopy only after decontamination with 4% paraformaldehyde for a minimum of 1 h, according to an in-house validated and approved method of sample decontamination. Total RNA from SARS-CoV-2-infected cells was extracted and purified with the QIAGEN RNeasy Mini Kit.

### QUANTIFICATION AND STATISTICAL ANALYSIS

The data was statistically analyzed using the Graph Pad Prism version 9.0 software. The numerical results are presented as mean standard deviation. Quantitative data in histograms, line charts and individual data points were presented as mean $\pm$ SEM. Statistical analyses were performed using two-tailed unpaired Student's t-tests. $p < 0.05$ was the criterion for statistically significant group differences.